Microfluidics-based analysis of dynamic contact angles relevant for underground hydrogen storage

Willemijn van Rooijen

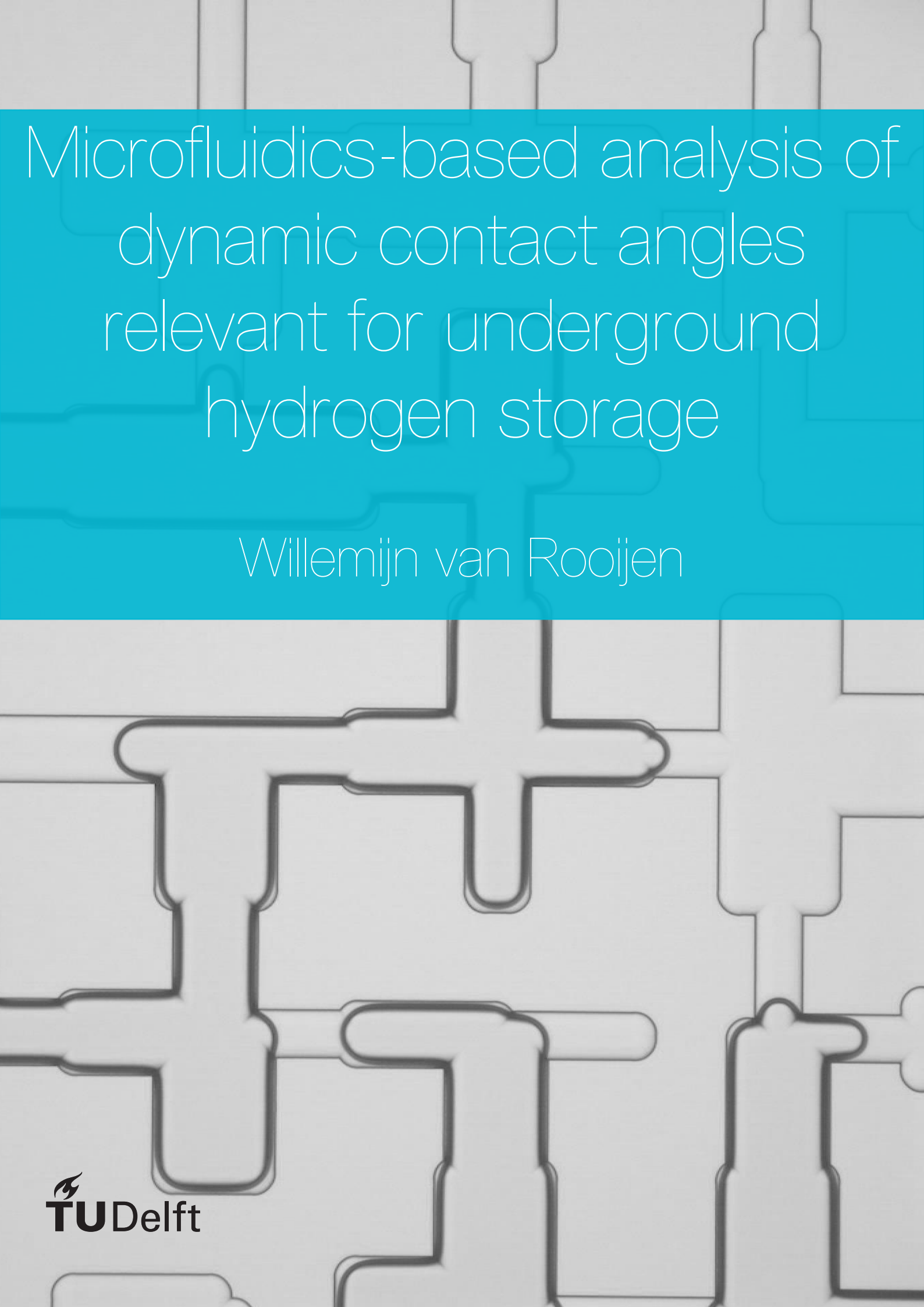

TU Delft

Microfluidics-based analysis of dynamic contact angles relevant for underground hydrogen storage

by

Willemijn van Rooijen

to obtain the degree of Master of Science
at the Delft University of Technology,
to be defended publicly on Monday November 15, 2021 at 15:00.

Student number: 4372999
Project duration: February 1, 2021 – November 15, 2021
Thesis committee:

Dr. H. Hajibeygi,	TU Delft, main supervisor
L. Hashemi,	TU Delft
Dr. M. Boon,	TU Delft
Dr. R. Farajzadeh,	TU Delft
Dr. V. van Steijn,	TU Delft

TU Delft

Preface

In January 2021 the opportunity for this master project came along. The fact that it involved experimental research made me particularly enthusiastic. Even though performing experimental research posed its own challenges, spending all these months in the lab gave me a deeper understanding of how things work in practice, which is very valuable to me.

During this master thesis project I was lucky to receive excellent support, for which I would like to express my gratitude. First of all, I would like to thank Hadi Hajibeygi. Not only for his very useful supervision, but also for the conversations about my future and the opportunity to continue with a PhD. Hadi Hajibeygi was sponsored by Dutch National Science Foundation (NWO) under Vidi Project "ADMIRE" (grant number 17509). Secondly, I thank Leila Hashemi and Maartje Boon for their supervision and help with the experiments. I also gratefully thank Michiel Slob for enabling me to perform the experiment through his support in the laboratory. A large thanks to Sian Jones as well, for helping me during practical challenges in the laboratory. I would like to show my appreciation to Cas and Wuis for their presence in the lab during the quiet Corona period. Thank you Rouhi Farajzadeh for the advice in the weekly meetings. Last, but not least, I would like to thank my family, friends and of course my boyfriend Matthijs for the support during this master thesis project and my entire time at the TU Delft.

Willemijn van Rooijen
Delft, November 2021

Abstract

Underground Hydrogen storage (UHS) is an attractive technology for large-scale energy storage. The UHS safety and efficiency depends highly on accurate characterization of H_2 interactions with reservoir fluids, specially wettability analyses for H_2/brine/rock systems. This thesis reports experimental measurements of advancing and receding contact angles of H_2/water, N_2/water and CO_2/water systems at P = 10 bar and T = 20 °C using a microfluidic chip (channel widths: 50 - 130 µm). The results indicate strong water-wet conditions with H_2/water advancing and receding contact angles of respectively 13 - 39°, and 6 - 23°. It was found that the contact angles decrease with increasing channel widths. Little hysteresis was measured, and consequently, the results are not in line with Morrow's curve. The receding contact angle measured in the smallest channel agrees well with the literature coreflood tests. The N_2/water and CO_2/water systems showed similar behaviours as the H_2/water system.

Contents

List of Figures

List of Abbreviations

ACA	Advancing contact angle
ICA	Intrinsic contact angle
RCA	Receding contact angle
SCA	Static contact angle
UHS	Underground hydrogen storage

Nomenclature

Θ	Contact angle
Θ_A	Advancing contact angle
Θ_R	Receding contact angle
Θ_S	Static contact angle
σ	Interfacial tension
σ_{nws}	Interfacial tension between non-wetting phase and solid phase
σ_{wnw}	Interfacial tension between wetting phase and non-wetting phase
σ_{ws}	Interfacial tension between wetting phase and solid phase
c	Constant
n	Order of polynomial
P	Pressure
P_C	Capillary pressure
P_{nw}	Pressure of the non-wetting phase
P_w	Pressure of the wetting phase
r	Radius
r_1	Radius of curvature in first direction
r_2	Radius of curvature in second direction

1

Introduction

Contribution of renewable energy, especially wind and solar, in the future global energy mix is expected to increase significantly [9]. However, due to the intermittent nature of these energy resources, development of large-scale (TWh) energy storage systems are essential components of future green energy systems [10]. Hydrogen (H_2) is considered as an attractive energy carrier because of its high mass energy density (i.e., 120 MJ/kg) and its clean combustion products. However, because of its low density (i.e., 0.09 kg/m^3 at standard conditions), surface-based storage facilities do not offer the volumes required for large-scale (Twh) energy storage. Geological formations, such as depleted oil and gas reservoirs, aquifers or salt caverns; on the other hand, offer feasible solutions [5, 10–12] (Figure 1.1). A list of all operational projects can be found in the recent UHS literature [5, 12]. A literature study on the disciplines of UHS and its main risks can be found in Appendix A

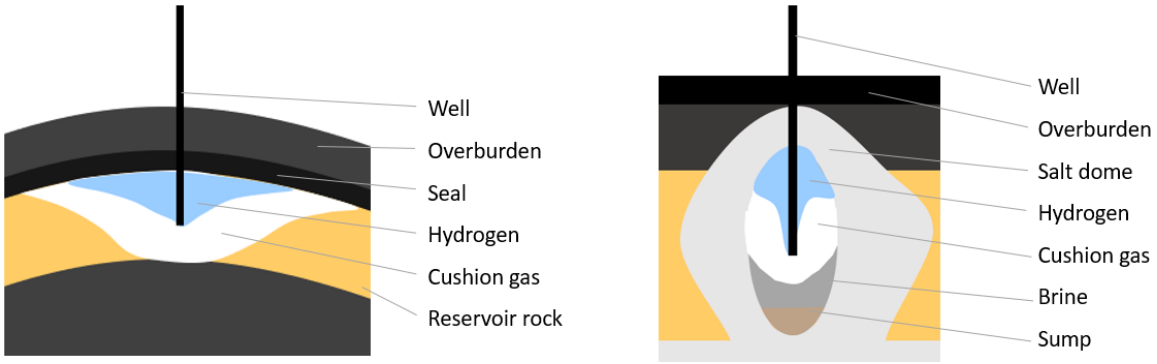

Figure 1.1: Schematic drawing of UHS in geological formations: depleted oil or gas reservoirs and aquifers (left) and salt caverns (right)

A good understanding of H_2/water transport properties such as relative permeability and capillary pressure is needed to ensure the safety of Underground Hydrogen Storage (UHS), as well as to optimize injection and withdrawal cycles [3, 10, 13–16]. Relative permeability and capillary pressure functions are highly dependent on the wetting properties of the system [1, 3, 17]. The wettability in H_2/brine/rock systems can be characterized by the contact angle between the rock-brine and the brine-H_2 interfaces (Section 3.1 Fig 2.2).

Contact angles can be directly measured experimentally using captive bubble method [5, 18], Sessile drop method [19–21], Capillary tubes [22–25], Tilted plate method [26], Wilhelmy plate method [27], Microfluidic chips [8, 25], and In-situ µCT measurements [21, 28], of which µCT measurements of the contact angles are most representative for local pore geometries. To the best of our knowledge, there is only limited experimental data available on H_2 contact angles in subsurface systems. Moreover, no direct measurements to quantify the effect of pore size on this parameter has been reported.

Yekta et al. [7] performed core-flooding tests, in which hydrogen was injected into a water-saturated Vosges sandstone rock, to derive drainage relative permeability and capillary pressure curves. The

experiments were carried out to represent shallow (50 bar - 20 °C) and deep (100 bar - 45 °C) aquifers. By combining the capillary pressure results with mercury injection capillary pressure (MICP) measurements and using the Young-Laplace scaling, they found receding contact angles of 21.6° and 34.9° for the first and second conditions, respectively. Iglauer et al. [6] used the tilted plate experimental technique to determine advancing and receding contact angles for the H_2/brine/quartz system. The experiments were performed for a pressure range of 50-250 bar, and a temperature range of 23-70 °C. A brine with a salinity of 100,000 ppm NaCl was used. They found that increasing pressure, temperature, and organic surface concentration increased the hydrogen wettability, with contact angles ranging between 0° to maximum 50°. Lastly, Hashemi et al. [3] performed static contact angle measurements for H_2/brine/sandstone rock using a captive-bubble cell device. No meaningful correlations were found by changing pressure (20 - 100 bar), temperature (20 - 50 °C) and salinity (0 - 50 000 ppm NaCl) of the brine. Intrinsic contact angles between 25° (min) to 45°(max) were found for a variety of tests.

Although, water-wet conditions were commonly found in all the past experiments, there still exist some inconsistencies between the currently reported data, which then leave uncertainties as to what the in-situ H_2 contact angles are in the realistic subsurface systems. This could possibly be explained by differences in the measurement techniques and types of rocks and fluids used in the experiments. To help shedding new lights on characterisation of this crucial interface property, a systematic study is reported in this paper, for a transparent dynamic multiphase flow system. More precisely, in this work, we measure contact angles in microfluidic systems for both drainage (receding) and imbibition (advancing) processes. Microfluidic chips resemble actual subsurface systems much closer compared to tilted plate techniques or captive bubble cells, because of the dynamic and micro-channel-based nature of the flow conditions.

Because H_2 will be periodically injected and produced from the reservoir, drainage and imbibition processes will alternately occur in the real system. The hysteresis in contact angles, and thus relative permeability and capillary pressure curves, has direct impact on the amount of residual and capillary-trapped non-wetting phase [29], in this case H_2. Because trapped H_2 cannot be produced from the reservoir, the trapping of H_2 is disadvantageous for the economic feasibility of UHS.

Morrow [4] investigated the dependence of the advancing and receding contact angles on intrinsic contact angles by measuring intrinsic contact angles on a smooth PTFE surface for a range of systems consisting of different fluid pairs, while the corresponding advancing and receding contact angles were measured in PTFE tubes. The study showed a systematic dependency of the advancing and receding contact angles on the intrinsic contact angle. The study is referred to as the Morrow curve in the current paper (Fig. 4.3). The Morrow curve can be used to predict the hysteresis behavior based on the intrinsic contact angle.

Microfluidic investigations can provide insight in the dynamics of fluid flow, interfacial tension and mass transfer [30]. Microfluidics experiments at early stages were based on simple micromodels, but later involved more complex network geometries [30]. The main limitations of most micromodels, however, include their restriction to 2D networks, their uniform etch depth, and uniform surface chemistry and minimum channel width of 10µm [31]. There are a few examples of the micromodels which resemble actual 3D rock systems more closely [32, 33]. Micromodels have widely been used for experiments on wettability [31, 34–36]. However, to the best of the authors' knowledge, the study conducted by Jafari and Jung [8] is the only one which has employed a micromodel to directly measure dynamic contact angles in randomly-patterned channels.

The objective of this work is to characterize dynamic contact angles, and also to quantify the impact of pore size on wettability in a H_2/water/glass system. The results reported in this study can be directly used in the pore-scale modelling of UHS such as the one performed by Hashemi et al. [5], in order to find relative permeability and capillary pressure curves.

The rest of the thesis is structured as follows. First, background theory will be provided. Then the experimental setup and procedure will be described, followed by the method of image analysis. Then, the results and their relevance for UHS will be provided and discussed. Finally, concluding remarks will be presented.

2

Theory

2.1. Interfacial tension, wettability and contact angle

When a liquid is in contact with another liquid (inmiscible with each other) or solid, there is a free interfacial energy present. This interfacial tension arises due to the difference in inward attraction of the molecules of both phases present. The free energy per unit area of the surface between the phases is defined as the interfacial tension (σ). [1, 17].

The wettability is a measure of the ability of a fluid to interact with a solid surface in combination with another fluid. This can be represented by the contact angle. The contact angle is defined as the angle that a two-fluid interface makes with the solid surface. A contact angle < 90 °defines the non-wetting phase, while a contact angle > 90°defines the wetting phase, see Figure 2.1 [1, 17].

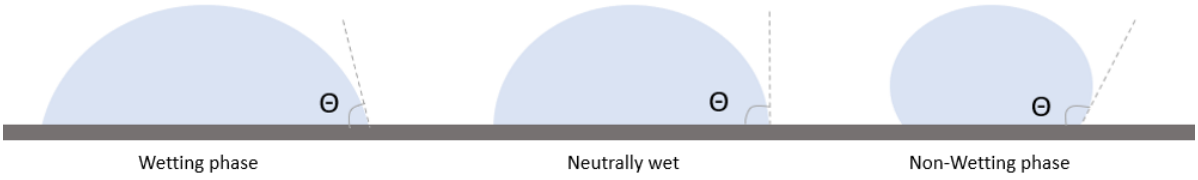

Figure 2.1: Schematic drawing of wetting and non-wetting phases.

The contact angle is static (SCA) when the interface is not moving. Dynamic contact angles (DCA) can be measured during imbibition, where the wetting phase is displacing the non-wetting phase. Such a process leads to advancing contact angles (ACA). Alternatively, they can be measured during drainage, where the non-wetting phase is displacing the wetting phase. This experiment corresponds to receding contact angles (RCA). An illustration is provided in Fig 2.2. Hysteresis is then defined as the difference between the advancing and receding contact angles [37]. When the surface is smooth and the fluids are at rest and free of polar impurities, the contact angle is a fundamental property of the system. This is called the intrinsic contact angle (ICA) [4]. As shown in Figure 4.3, Morrow's curve [4] shows a systematic dependence of the advancing and receding contact angles on the intrinsic contact angle.

The contact angle is directly depending on the interfacial tension between: 1) the wetting phase and the non-wetting phase, 2) wetting phase and the solid, and 3) the non-wetting phase and the solid (Figure 2.3). This is defined by Young's equation [1, 17, 38]:

$$cos\theta = \frac{\sigma_{nws} - \sigma_{ws}}{\sigma_{wnw}} \tag{2.1}$$

where ϑ is the contact angle, σ_{nws}, is the interfacial tension between the non-wetting phase and the solid, σ_{ws}, is the interfacial tension between the wetting phase and the solid and σ_{wnw}, is the interfacial tension between the wetting phase and non-wetting phase.

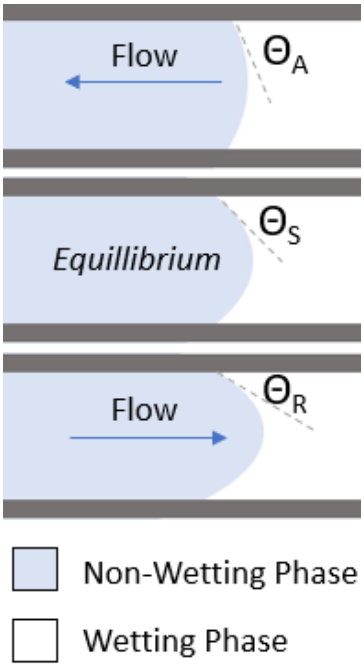

Figure 2.2: Schematic drawing showing the interface between the wetting and non-wetting phase. The advancing (ACA) and receding contact angles (RCA) are indicated by Θ_A and Θ_R, respectively. The static contact angle is illustrated by Θ_S.

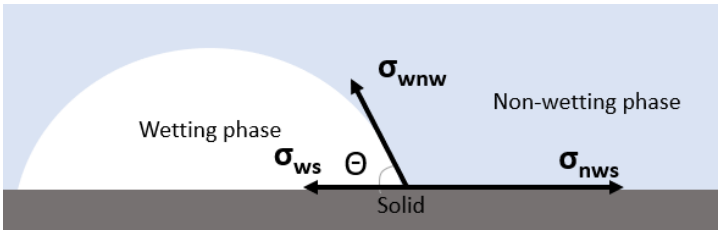

Figure 2.3: Interfacial tension and contact angle of Young's equation. (ϑ is the contact angle, σ_{nws}, is the interfacial tension between the non-wetting phase and the solid, σ_{ws}, is the interfacial tension between the wetting phase and the solid and σ_{wnw}, is the interfacial tension between the non-wetting phase and non-wetting phase)

2.2. Capillary pressure

When two fluids are in contact with a solid, the interface of the fluids is curved. The reason for this is that one of the fluids, the wetting fluid, has a larger preference to wet the solid. The curvature of the interface leads to a pressure difference between the two fluids, called the capillary pressure (P_c). The non-wetting phase has a higher pressure, it does not prefer the solid and needs more pressure to be moved through a tube or a porous medium [1, 17, 38].

The Young-Laplace equation relates the capillary pressure to the curvature of the interfaces:

$$P_c = P_{nw} - P_w = \sigma\left(\frac{1}{r_1} + \frac{1}{r_2}\right) \tag{2.2}$$

where P_{nw} is the pressure of the non-wetting fluid, P_w is the pressure of the wetting fluid, σ is the interfacial tension and r_1 and r_2 are the principal radii of curvature as indicated in Figure 2.4

The Laplace equation can be rewritten for specific cases. For example, in case of a circular capillary tube, the radii of curvature are the same so $r_1 = r_2$. It can be derived by using trigonometry that $r_1 = r_2 = r/\cos\vartheta$, where r is the radius of the capillary tube (Figure E). Combining this with the Young-Laplace equation gives [1, 17, 38]:

$$P_c = P_{nw} - P_w = \frac{\sigma cos\theta}{r} \tag{2.3}$$

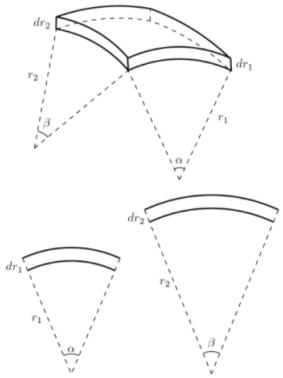

Figure 2.4: Schematic drawing of a small part of an interface between two fluids, which has two principal radii of curvature: r_1 and r_2 [1].

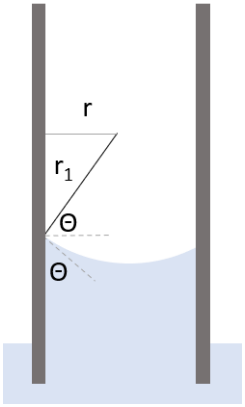

Figure 2.5: Schematic drawing of a capillary tube. Here, r is the radius of the tube, r_1 is the radius of curvature and ϑ is the contact angle.

2.3. Influence of intermolecular forces on contact angles

As stated in section 2.1, the contact angle is directly dependent on the interfacial tension values of the interfaces present in the system. The interfacial tension is the energy penalty for breaking the intermolecular forces within the phases itself and creating an interface between the two phases. This energy penalty is largest if there is a big difference in intermolecular forces present within both phases.

A similar example to hydrogen/water, an oil water system, is shown in Figure 2.6. Because a water molecule is a dipole, it can form strong dipole-dipole bonds, hydrogen bonds, which are represented by the solid arrows. Oil on the other hand has, just like hydrogen, non-polar molecules, and therefore only weaker Van der Waals forces are present between molecules, which are represented by the dashed lines. If oil or hydrogen needs to form an interface with water, strong hydrogen bonds are broken and replaced by weak Van der Waals forces [1]. This results in a relatively large interfacial tension.

In this research silica/hydrogen/water contact angles are measured. Silica is a solid with strong interatomic bonding, so high surface energy is expected to result from breaking these bonds. As stated above, water has stronger intermolecular bonds than hydrogen and therefore the strength of the water bonds is closer to the strong interatomic bonding of silica. This results in a lower interfacial tension between silica and water than between silica and hydrogen. Consequently, water is the wetting phase in this system [1].

2.4. Relative permeability

Relative permeability is defined as the ability of a porous medium to conduct a fluid when more than one fluid is present [38]. The relative permeability is dependent on the saturation, pore shape, wettability and fluid distribution. It was found by Owens and Archer [2] that contact angle can have significant

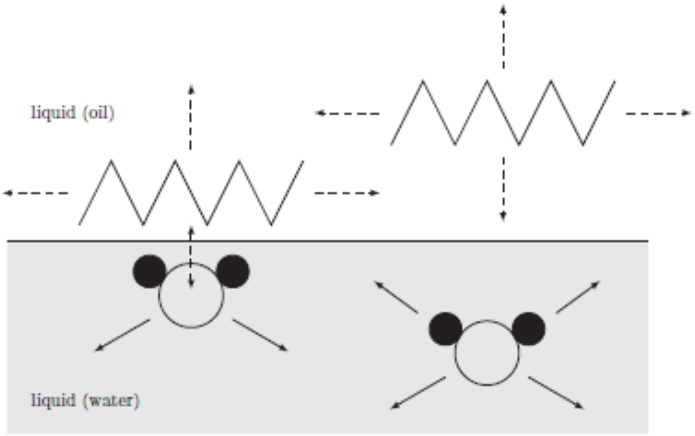

Figure 2.6: Schematic drawing of forces present at the interface of water and oil. The oil molecules are only bounded by weak Van der Waals intermolecular forces dashed arrow, whereas the water moleculer are bonded by strong hydrogen bonds (solid arrow). At the interface hydrogen bonds are broken and replaced by weak Van der Waals forces [1].

influence on the relative permeability in oil/water systems (Figure 2.7).

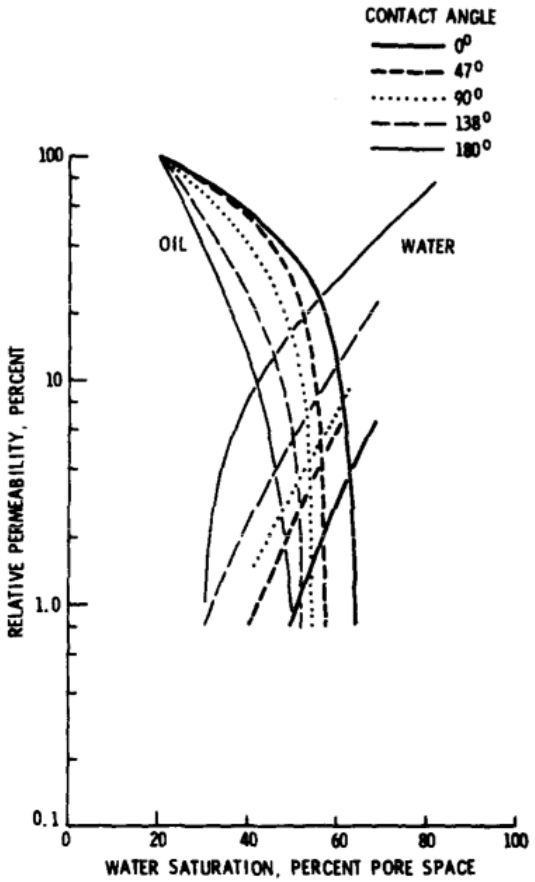

Figure 2.7: Influence of wettability on relative permeability found by Owens and Archer [2].

3

Materials and Methods

In this study, microfluidic chips are utilized to measure dynamic contact angles of gas-solid-liquid interfaces for the H_2/water, N_2/water, and CO_2/water systems. Data sets on wettability of systems containing N_2 and CO_2 are more widely available than H_2. These data sets were then used to calibrate our setup and to investigate the influence of the solubility of the gas on the measured data. The experimental test groups and conditions are summarized in Table 3.1. The advantage of using microfluidic chips is that the in-situ dynamic contact angles can be measured in channels with widths that are representative of porous media in the subsurface formations.

3.1. Materials

The microfluidic device used in the experiments consisted of a microchip (10 x 20 mm) supplied by Micronit Company. The material of the chip is borosilicate glass, and it has a pattern of a random square network. The channels had maximum widths of 50, 70, 90, 110 and 130 µm, of which the smallest channel width was in the range of the most common pore sizes of Berea and Bentheimer sandstones [3, 39]. The depth of the channels is 20 µm. The shape of the channels is near-rectangular, with edged sides at the bottom. An overview of the chip can be found in Fig. 3.1. H_2, N_2 and CO_2 gas with respective purity of 99.99%, 99.7% and 99.7% were used. Deionized degassed water was used during the experiments.

3.2. Experimental apparatus

Figure 3.2 provides a schematic overview of the microfluidic apparatus. The microscope is a Leica DMi8 DFC7000 and was used in combination with an objective with a magnification of 10X to visualize the experiments. Videos of the experiments were taken with a Leica DFC7000T camera with LAS software. The frame rate of the videos was approximately 5 frames per second. To prevent the chip from being contaminated, multiple filters were incorporated in the apparatus. The injected water (and ethanol) was filtered with a 0.2 µm VICI filter. In addition, there were two extra 0.5 µm filters (VICI Jour PEEK-encased frits) installed in the liquid and gas lines. Two pumps were included in the setup, a quizix QX6000 pump and a PHD Ultra™ 4400 Programmable Syringe Pump - Harvard Apparatus with a 250 µL syringe. The Quizix pump was used to refill the highly accurate syringe pump, which can deliver flowrates down to nanolitres/min, while the syringe pump was used for the injection into, and the withdrawal from the microchip. The valves installed (Swagelok) were 1/16” and 0.25 mm ID FEP transparent tubes were used. The gas cylinder served to maintain the pressure. The pressure was monitored by the Quizix Pump. The setup was calibrated against the existing literature data of Jafari and Jung [8]. The results

Test Group	Gas	Liquid	Rate [µl/min]	Temperature [°C]	Pressure [bar]
A	H_2	Pure Water	0.1	20	10
B	N_2	Pure Water	0.1	20	10
C	CO_2	Saturated Water	0.1	20	10

Table 3.1: Summary of the test groups and experimental conditions.

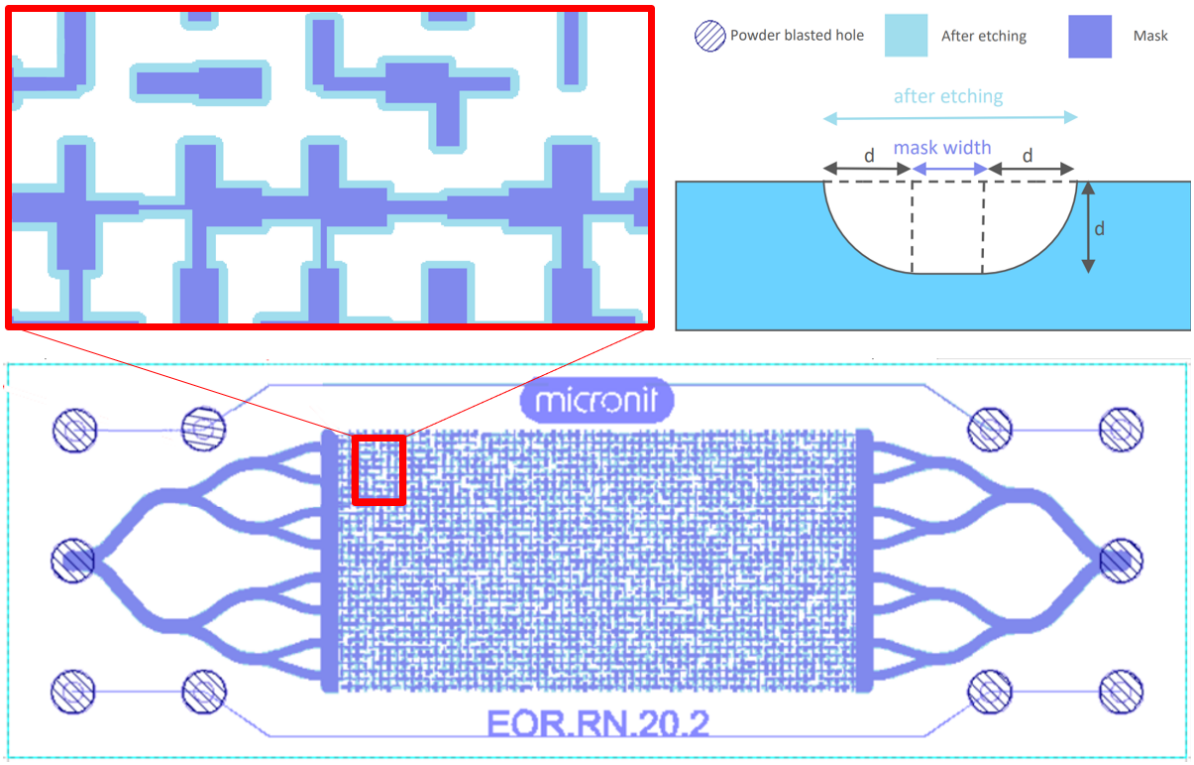

Figure 3.1: Schematic drawing of the borosilicate glass chip (based on the drawing on the website of Micronit Company). The chip is 10 mm × 20 mm. The channels have maximum widths of 50, 70, 90, 110 and 130 µm and the depth of the channels is 20 µm.

of the validation tests are described in detail in Appendix A. Another experimental apparatus using capillary tubes instead of microchips is tested and the findings are described in Appendix E.

3.3. Experimental procedure

To avoid the impact of possible contamination on the contact angle measurements the microchips were thoroughly cleaned prior to the measurements. The cleaning procedure involved rinsing the chips with 5 mL of filtered ethanol, followed by flushing with filtered N_2 until no liquid was visible in the chip. The cleaning procedure was carried out at ambient pressure.

To remove the N_2 from the clean chip, the system was flushed with the gas used in the experiment, followed by thoroughly rinsing and thereby saturating the chip with deionized water. This formed the starting point of the drainage tests. For most experiments, the chips were saturated with deionized water at ambient pressure. However, for the experiments where the deionized water was pre-equilibrated with CO_2 (see Table 3.1), the system was saturated at the experimental pressure of 10 bar to avoid exolution of dissolved CO_2 from the water. For these experiments, back-pressure regulators were installed at the outlets of valves 2 and 5.

At the start of the drainage tests, the system was pressurized to 10 bar and water was withdrawn from the water-saturated chips with a flow rate of 0.1 µL/min (corresponding to interstitial velocity ≈ 10^{-4} m/s). The drainage tests were followed by imbibition tests for which the chip was first thoroughly flushed with the corresponding gas of the experiment. The flushing was carried out at the ambient pressure, except for the experiments in which the deionized water was equilibrated with CO_2. For this experiment the flushing pressure was kept at 10 bar. This resulted in a system filled with gas and residual water. Next, the system was pressurized and, with a flow rate of 0.1 µL/min, water was injected into the microchip. During the experiments, videos were taken to capture the moving gas-water interfaces within the channels.

A detailed step-by-step experimental procedure is described in Appendix F.

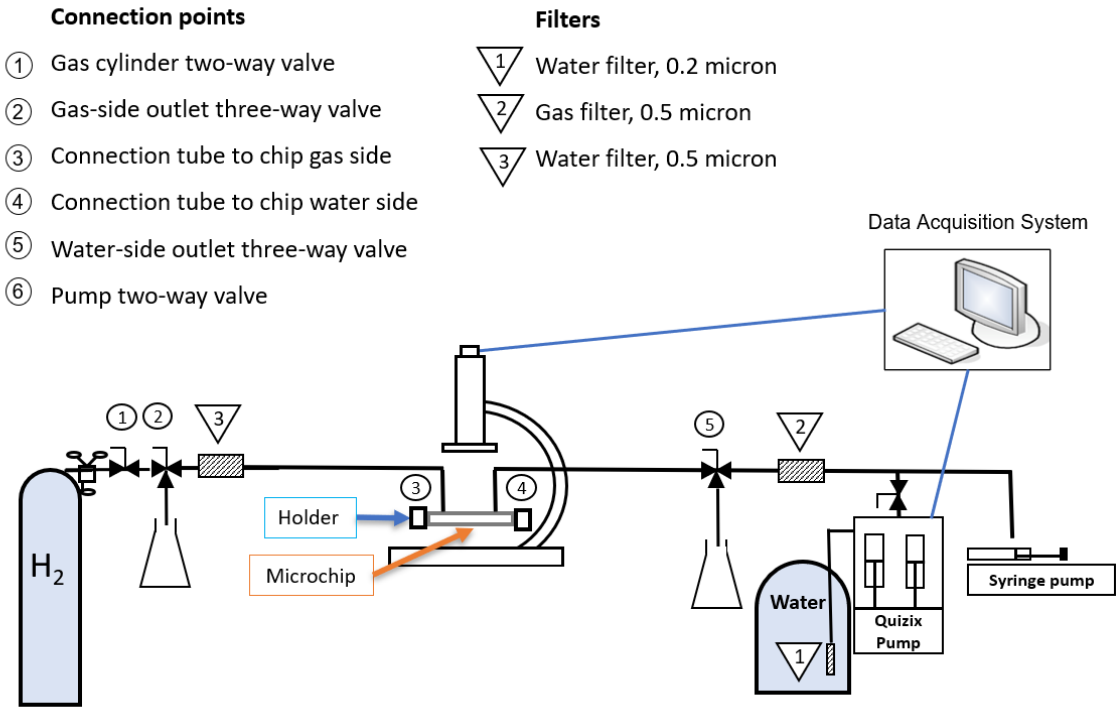

Figure 3.2: Schematic drawing of the experimental apparatus used to measure dynamic contact angles in microfluidic chips.

3.4. Image analysis

To calculate the dynamic contact angles, several snapshots from videos of the moving gas-water interfaces in different channel widths were captured. Snapshots were taken at locations where the interfaces met the following requirements: 1) the interface is moving, 2) the interface is not too close to the corners of the channels, and 3) the meniscus is sharp enough. Furthermore, only one snapshot per straight channel was taken to obtain a good representation of the whole chip.

The images were analyzed using an in-house MATLAB code. To process an image, first it was converted to the grey-scale format and the desired interface within a channel was cropped. Then, by using the scale factor of the microscope and selecting two points on the channel walls, the channel width was identified. To detect the boundary of the meniscus, the cropped section of the image was binarized and contact points, in addition to the apex, were identified. The best polynomials on each half of the curvature were fitted by both minimizing the error at the contact points (RMSE) and choosing a polynomial that optimally fits the meniscus <. All the steps of the image analysis are shown in Figure 3.3.

Contact angles are found first by fitting a polynomial of order n on the image, i.e.:

$$Z = c_1 R^n + c_2 R^{(n-1)} + c_i R^{n-(i-1)} + \ldots + c_{(n+1)}. \tag{3.1}$$

Here, c_i coefficients are constants, allowing the Z curve to be found as a function of R. Naturally, the derivative of Z with respect to R reads:

$$\frac{dZ}{dR} = n c_1 R^{(n-1)} + (n-1) c_2 R^{(n-2)} + \ldots + c_{(n)}. \tag{3.2}$$

As such, the contact angle θ is found at the gas/liquid/solid contact point according to the following equation:

$$\theta = \frac{\pi}{2} - tan^{-1}(\frac{dZ}{dR}). \tag{3.3}$$

As shown in Figure 3.3e, the origin of the coordinate system was placed at the apex point. The Z-axis is parallel to the flow direction and the R-axis perpendicular to the flow direction. Therefore, by solving Equation 3.1, 3.2 and 3.3, at the contact points the contact angle (θ) can be found. A validation of the image analysis code is provided in Appendix B.

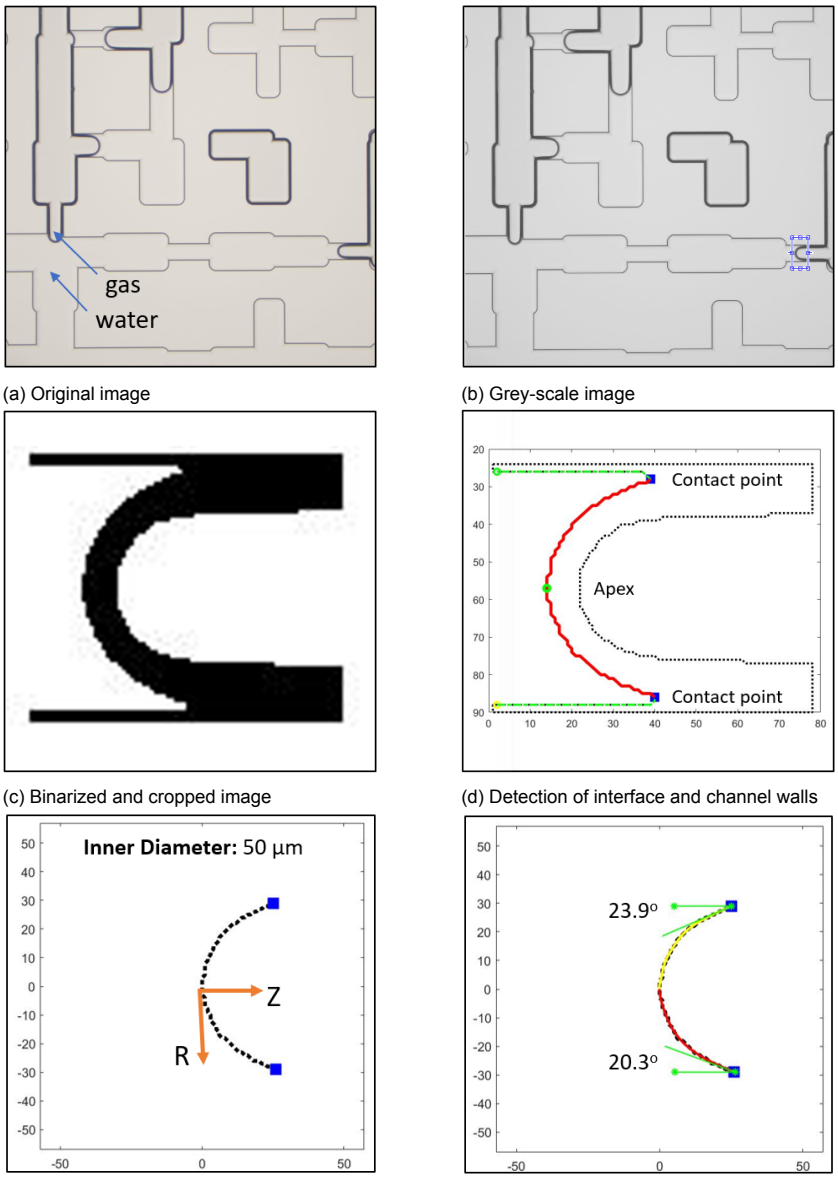

(a) Original image

(b) Grey-scale image

(c) Binarized and cropped image

(d) Detection of interface and channel walls

(e) Curvature from image

(f) Fitted 6th order polynomial on curvature

Figure 3.3: Procedure of the image analysis to identify the contact angles.

4

Results and Discussions

4.1. Characteristics of the interface

During the drainage and imbibition microfluidic experiments for the H_2/water, N_2/water, and CO_2/water systems, different kind of interfaces were encountered. The main difference was in the existence or non-existence of visible water films. A water film is expected to be present in all cases [40], however, in some of our cases the water film was so thin that it was not visible with our camera resolution. During drainage, when the receding contact angles (RCA) were measured, water films were visible on both sides of the channel (Figure 4.1d). For the measurements of advancing contact angles (ACA) during imbibition, interfaces were observed both with and without visible water films (Figure 4.1a, 4.1b and 4.1c). The interfaces are very sensitive to contamination within the gas/water/glass system. The differences in contact angle measurements between clean and impure systems, as well as example pictures of the polluting particles can be found in Appendix C.

4.2. Contact angles for the H_2/water, N_2/water, and CO_2/water systems

Figure 4.2 shows the advancing and receding contact angles for the H_2/water, N_2/water and CO_2/water systems, at a pressure of 10 (±1) bar and a temperature of 20 (±2) °C (Test A, B and C), measured in channel widths varying from 50 to 130 µm. The error bars represent the standard deviation of the measurements. The intrinsic contact angle of H_2/water/sandstone, measured by Hashemi et al. [3] (P=20 bar and T=20 °C) is indicated by the horizontal dashed line. Pure water was used for the H_2 and N_2 experiments, while for the CO_2 experiments the water was pre-equilibrated with CO_2. This was done to exclude the impact of CO_2 dissolution into water on the contact angle measurements. The solubility of CO_2 into water is very high compared to H_2 and N_2.

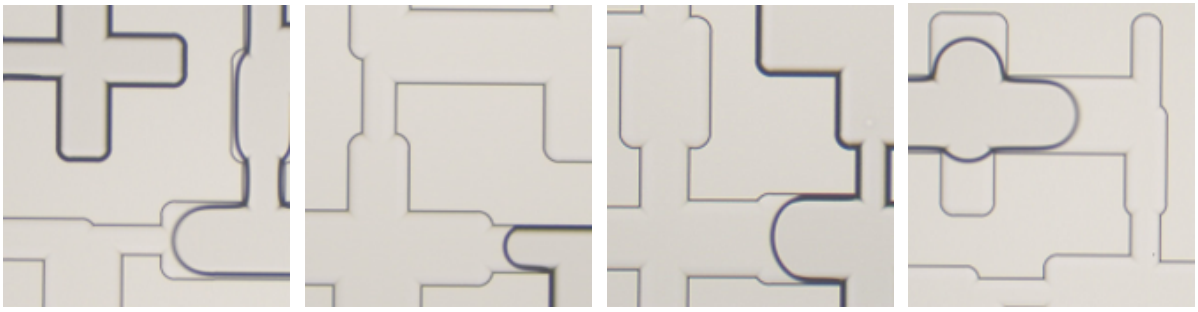

(a) ACA with water films visible on both sides.

(b) ACA with a visible water film on one side.

(c) ACA without visible water films.

(d) RCA with visible water films on both sides.

Figure 4.1: Types of interfaces encountered during imbibition when the advancing contact angle (ACA) is measured (a,b,c) and during drainage when the receding contact angle (RCA) is measured (d).

H_2/water receding contact angles of 6 - 2 ° and advancing contact angles of 13 - 39° were determined based on the microfluidic experiments. The highest angles were measured in the smallest channels and the lowest angles were measured in the widest channels. No significant difference in the receding contact angles was observed for the three different gases. The wider error bars of the advancing contact angles compared to the receding contact angles imply that the advancing contact angles are less reproducible. This can partly be explained by the different interfaces that formed during imbibition (Figure 4.1a, 4.1b and 4.1c). The advancing contact angles measured for the H_2/water system are larger (1 - 14°) compared to N_2/water and CO_2/water systems. However, the overlap in error bars shows that this difference is not evident and is within the experimental accuracy. This is because the error bars represent the standard deviation of the measurements, and the range in measurements is much larger than the measured difference between the gases.

The overlap in the error bars between advancing and receding contact angles for all cases studied indicates that hysteresis effects are not significant for the three gases used in the experiments. More research on the contact angle hysteresis at reservoir conditions and using more realistic pore network, like micro-CT or core samples is required to confirm our findings. However, the lack of hysteresis in the H_2/rock system would be beneficial for UHS, since smaller amounts of H_2 will be trapped during multiple injection/production cycles of the UHS projects.

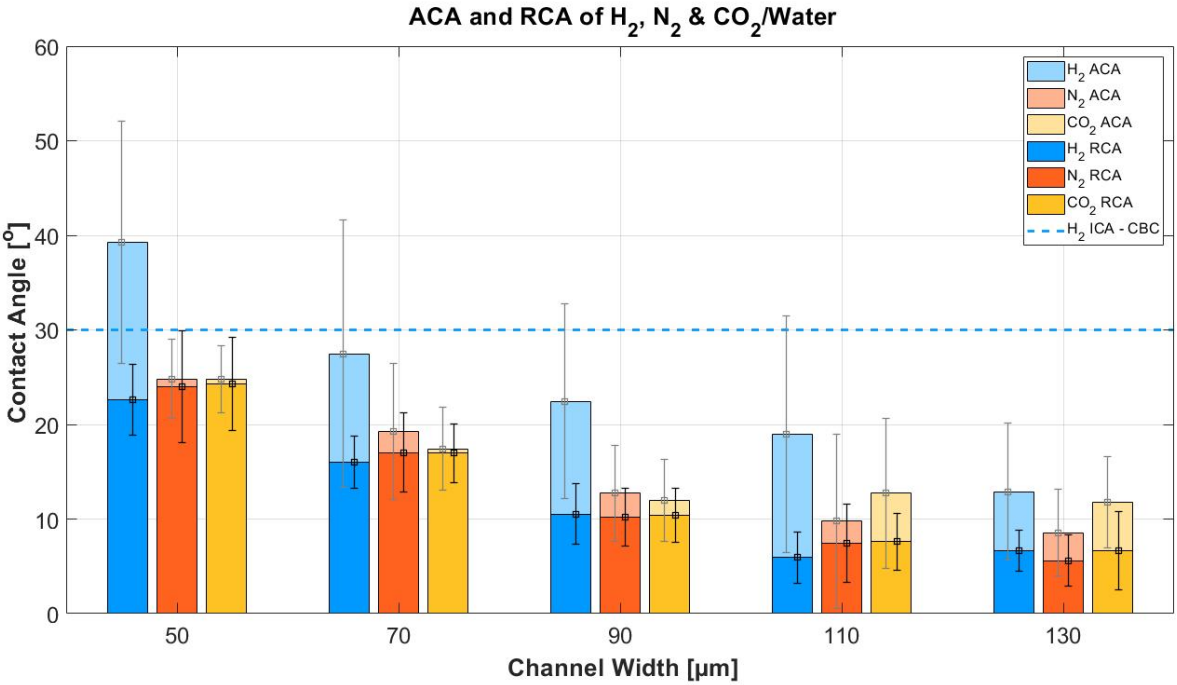

Figure 4.2: Advancing and receding contact angles (ACA and RCA) of H_2/water, N_2/water and CO_2/water at P=10 bar and T=20 °C. Pure water was used for measurements of H_2 and N_2 and for the experiment of CO_2 the water was pre-equilibrated with CO_2. The dashed blue line represents the results found by Hashemi et al. [3] at P=20 bar and T=20 °C using the captive bubble cell (CBC). The error bars represent the standard deviation of the measurements.

4.3. H_2/water contact angles compared with literature

Figure 4.3 compares the findings on H_2/water dynamic contact angles, both advancing and receding, with the currently available literature data on the dynamic contact angles measured for the H_2/water system. The left graph shows the relationship between the advancing and receding contact angles as functions of the intrinsic contact angle (ICA) based on the findings of Morrow [4]. The * indicates the modified relationship suggested by Hashemi et al. [5]. The vertical gray dashed line represents the intrinsic contact angle for the H_2/water/sandstone found by the captive-bubble experiments of Hashemi et al. [3] (P=20 bar and T=20 °C), referred to as CBC. According to the Morrow curve, this intrinsic contact angle corresponds to advancing and receding contact angles represented by the solid and dashed horizontal blue lines, respectively. The same solid and dashed horizontal blue lines are visible

in the bar plot on the right side of Figure 4.3. The bar plot shows the dynamic contact angles for the H_2/water system measured with the microfluidic device of this study (Test C) for channel width ranging from 50 to 130 µm. In addition, the H_2/brine/quartz results of the tilted plate experiment of Iglauer et al. [6] (P=50 bar, T=23 °C and Sal. = 100 000 ppm), referred to as TPM, and the H_2/water/sandstone core flooding experiment of Yekta et al. [7] (P=50 bar and T=20 °C), referred to as CF, are presented.

The advancing and receding contact angles obtained with the Morrow curve and based on the intrinsic contact angle of the H_2/water of Hashemi et al. [3] are 16.5° and 0.8°, respectively. The value of the advancing contact angle corresponds closest to the results of the channel widths of 110 and 130 µm. However, as previously stated, little hysteresis in contact angles was observed with the mircofluidic device and conditions of this study. As a result, the Morrow curve does not represent the behaviour seen during these microfluidic experiments and cannot be used to predict the hysteresis. When comparing the results of Iglauer et al. [6] with the results of our microfluidic experiment, it can be seen that the receding contact angles of both experiments are the same. The advancing contact angles, however, differ by 5°. In both experimental methods, the advancing contact angles are found to be less reproducible, which could explain the difference. The receding contact angle found by Yekta et al. [7] is very similar to the receding contact angle measured in channels of 50 µm in width, with only 1° difference. Yekta et al. [7] used a Vosges Sandstone for the core flooding experiment. It is possible that the common pore-sizes in this sandstone are in the range of 50 µm, similar to Bentheimer and Berea sandstone [5, 39].

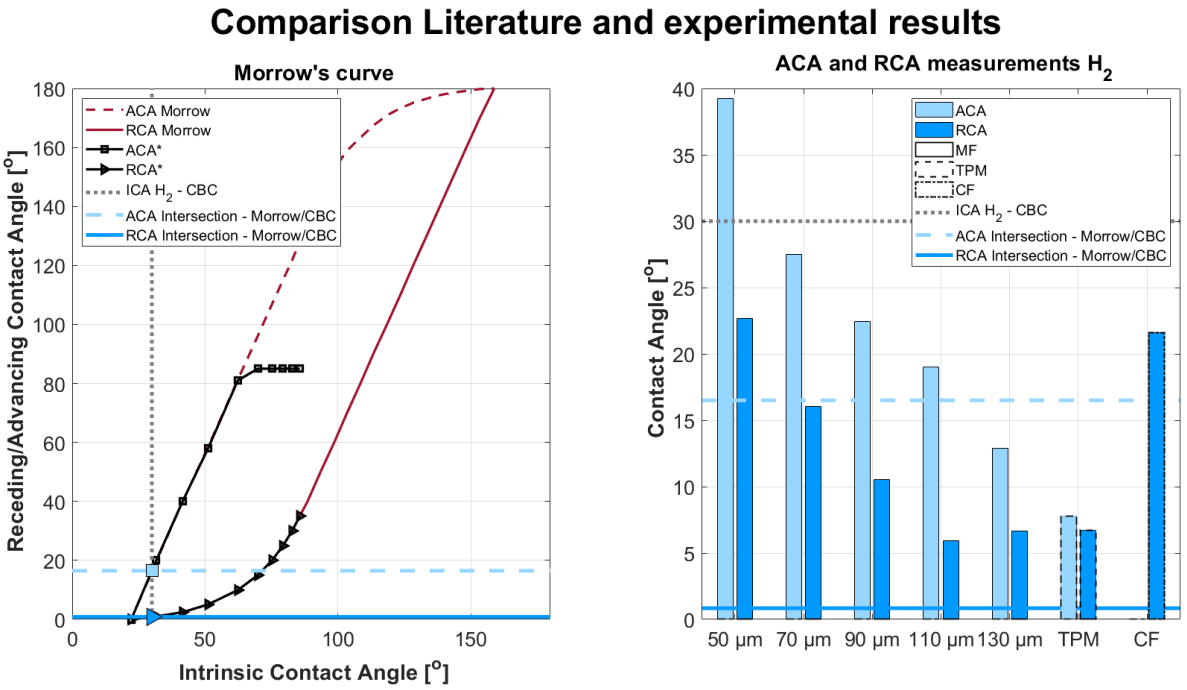

Figure 4.3: Left: The Morrow curve based on the findings of Morrow [4], the * indicates the modified relationship suggested by Hashemi et al. [5] and the intrinsic contact angle (ICA), indicated by the gray dashed line, is based on the findings of Hashemi et al. [3] using the captive bubble method (CBC). The solid and dashed blue horizontal lines are the intersections between the ICA of CBC and Morrows curve, which represent the RCA and ACA, respectively. Right: H_2/water advancing and receding contact angles for channel widths of 50 to 130 µm found by the microfluidic experiments of this study (MF). The results of the tilted plate method of Iglauer et al. [6] (TPM), and the core flooding method of Yekta et al. [7] (CF), are represented by the bars on the right.

5

Conclusions

Prediction of rock wettability in contact with brine and hydrogen is crucial for modelling the displacement processes in underground hydrogen storage (UHS). This thesis reports experimental measurements of the advancing and receding contact angles of H_2/water, N_2/water and CO_2/water systems at P = 10 bar and T = 20 °C using a microfluidic device. The channel widths of the microfluidic chip, ranged between 50 to 130 µm and the size of the smallest channel correspond to the range of most common pore-sizes found in typical sandstones [5, 39]. The results indicate water-wet conditions with H_2/water advancing contact angles ranging between 13 - 39 °, and receding contact angles between 6 - 23 °. The contact angles decreased with increasing channel widths. Little hysteresis was found and as a result the Morrow curve does not capture the behaviour observed in this study. The receding contact angle measured for the smallest channel width (50 µm) is in agreement width the receding contact angle determined by Yekta et al. [7] on the Vosges Sandstone, suggesting that this channel width is representative of actual subsurface systems. The N_2/water and CO_2/water systems showed similar behaviour to the H_2/water system and no significant differences were observed for the three different gases.

References

[1] M. J. Blunt, Multiphase flow in permeable media: A pore-scale perspective, Cambridge University Press, 2017.

[2] W. Owens, D. Archer, The effect of rock wettability on oil-water relative permeability relationships, Journal of Petroleum Technology 23 (1971) 873–878.

[3] L. Hashemi, W. Glerum, R. Farajzadeh, H. Hajibeygi, Contact angle measurement for hydrogen/brine/sandstone system using captive-bubble method relevant for underground hydrogen storage, Advances in Water Resources (2021) 103964.

[4] N. R. Morrow, The effects of surface roughness on contact: angle with special reference to petroleum recovery, Journal of Canadian Petroleum Technology 14 (1975).

[5] L. Hashemi, M. Blunt, H. Hajibeygi, Pore-scale modelling and sensitivity analyses of hydrogen-brine multiphase flow in geological porous media, Scientific reports 11 (2021) 1–13.

[6] S. Iglauer, M. Ali, A. Keshavarz, Hydrogen wettability of sandstone reservoirs: Implications for hydrogen geo-storage, Geophysical Research Letters 48 (2021) e2020GL090814.

[7] A. Yekta, J.-C. Manceau, S. Gaboreau, M. Pichavant, P. Audigane, Determination of hydrogen–water relative permeability and capillary pressure in sandstone: application to underground hydrogen injection in sedimentary formations, Transport in Porous Media 122 (2018) 333–356.

[8] M. Jafari, J. Jung, Direct measurement of static and dynamic contact angles using a random micromodel considering geological co2 sequestration, Sustainability 9 (2017) 2352.

[9] D. MacKay, Sustainable Energy-without the hot air, UIT cambridge, 2008.

[10] N. Heinemann, J. Alcalde, J. M. Miocic, S. J. Hangx, J. Kallmeyer, C. Ostertag-Henning, A. Hassanpouryouzband, E. M. Thaysen, G. J. Strobel, C. Schmidt-Hattenberger, et al., Enabling large-scale hydrogen storage in porous media–the scientific challenges, Energy & Environmental Science (2021).

[11] M. Ali, N. K. Jha, A. Al-Yaseri, Y. Zhang, S. Iglauer, M. Sarmadivaleh, Hydrogen wettability of quartz substrates exposed to organic acids; implications for hydrogen trapping/storage in sandstone reservoirs, Journal of Petroleum Science and Engineering (2021) 109081.

[12] D. Zivar, S. Kumar, J. Foroozesh, Underground hydrogen storage: A comprehensive review, International Journal of Hydrogen Energy (2020).

[13] M. Rücker, W.-B. Bartels, K. Singh, N. Brussee, A. Coorn, H. A. van der Linde, A. Bonnin, H. Ott, S. M. Hassanizadeh, M. J. Blunt, et al., The effect of mixed wettability on pore-scale flow regimes based on a flooding experiment in ketton limestone, Geophysical Research Letters 46 (2019) 3225–3234.

[14] P. Kunz, S. Hassanizadeh, U. Nieken, A two-phase sph model for dynamic contact angles including fluid–solid interactions at the contact line, Transport in Porous Media 122 (2018) 253–277.

[15] B. Pan, X. Yin, Y. Ju, S. Iglauer, Underground hydrogen storage: Influencing parameters and future outlook, Advances in Colloid and Interface Science (2021) 102473.

[16] P. Carden, L. Paterson, Physical, chemical and energy aspects of underground hydrogen storage, International Journal of Hydrogen Energy 4 (1979) 559–569.

[17] J. Bear, Dynamics of fluids in porous media, Courier Corporation, 2013.

[18] S. Saraji, M. Piri, L. Goual, The effects of so2 contamination, brine salinity, pressure, and temperature on dynamic contact angles and interfacial tension of supercritical co2/brine/quartz systems, International Journal of Greenhouse Gas Control 28 (2014) 147–155.

[19] J. L. Dickson, G. Gupta, T. S. Horozov, B. P. Binks, K. P. Johnston, Wetting phenomena at the co2/water/glass interface, Langmuir 22 (2006) 2161–2170.

[20] D. N. Espinoza, J. C. Santamarina, Water-co2-mineral systems: Interfacial tension, contact angle, and diffusion—implications to co2 geological storage, Water resources research 46 (2010).

[21] L. E. Dalton, D. Tapriyal, D. Crandall, A. Goodman, F. Shi, F. Haeri, Contact angle measurements using sessile drop and micro-ct data from six sandstones, Transport in Porous Media 133 (2020).

[22] X. Li, X. Fan, A. Askounis, K. Wu, K. Sefiane, V. Koutsos, An experimental study on dynamic pore wettability, Chemical Engineering Science 104 (2013) 988–997.

[23] M. Heshmati, M. Piri, Experimental investigation of dynamic contact angle and capillary rise in tubes with circular and noncircular cross sections, Langmuir 30 (2014) 14151–14162.

[24] E. Al-Zaidi, X. Fan, Effect of aqueous electrolyte concentration and valency on contact angle on flat glass surfaces and inside capillary glass tubes, Colloids and Surfaces A: Physicochemical and Engineering Aspects 543 (2018) 1–8.

[25] E. R. Castro, M. D. Tarn, P. Ginterová, H. Zhu, Y. Xu, P. Neužil, Determination of dynamic contact angles within microfluidic devices, Microfluidics and Nanofluidics 22 (2018) 1–11.

[26] M. Arif, M. Lebedev, A. Barifcani, S. Iglauer, Co2 storage in carbonates: Wettability of calcite, International Journal of Greenhouse Gas Control 62 (2017) 113–121.

[27] J.-H. Kim, H. P. Kavehpour, J. P. Rothstein, Dynamic contact angle measurements on superhydrophobic surfaces, Physics of Fluids 27 (2015) 032107.

[28] C. Sun, J. E. McClure, P. Mostaghimi, A. L. Herring, M. Shabaninejad, S. Berg, R. T. Armstrong, Linking continuum-scale state of wetting to pore-scale contact angles in porous media, Journal of colloid and interface science 561 (2020) 173–180.

[29] R. Juanes, E. Spiteri, F. Orr Jr, M. Blunt, Impact of relative permeability hysteresis on geological co2 storage, Water resources research 42 (2006).

[30] M. L. Porter, J. Jiménez-Martínez, R. Martinez, Q. McCulloch, J. W. Carey, H. S. Viswanathan, Geo-material microfluidics at reservoir conditions for subsurface energy resource applications, Lab on a Chip 15 (2015) 4044–4053.

[31] Y. Kim, J. Wan, T. J. Kneafsey, T. K. Tokunaga, Dewetting of silica surfaces upon reactions with supercritical co2 and brine: pore-scale studies in micromodels, Environmental science & technology 46 (2012) 4228–4235.

[32] N. S. K. Gunda, B. Bera, N. K. Karadimitriou, S. K. Mitra, S. M. Hassanizadeh, Reservoir-on-a-chip (roc): A new paradigm in reservoir engineering, Lab on a Chip 11 (2011) 3785–3792.

[33] W. Song, T. W. de Haas, H. Fadaei, D. Sinton, Chip-off-the-old-rock: the study of reservoir-relevant geological processes with real-rock micromodels, Lab on a Chip 14 (2014) 4382–4390.

[34] A. Sharbatian, A. Abedini, Z. Qi, D. Sinton, Full characterization of co2–oil properties on-chip: solubility, diffusivity, extraction pressure, miscibility, and contact angle, Analytical chemistry 90 (2018) 2461–2467.

[35] C. Chalbaud, M. Robin, J. Lombard, F. Martin, P. Egermann, H. Bertin, Interfacial tension measurements and wettability evaluation for geological co2 storage, Advances in water resources 32 (2009) 98–109.

[36] R. Hu, J. Wan, Y. Kim, T. K. Tokunaga, Wettability effects on supercritical co2–brine immiscible displacement during drainage: Pore-scale observation and 3d simulation, International Journal of Greenhouse Gas Control 60 (2017) 129–139.

[37] B. E. Rapp, Microfluidics: modeling, mechanics and mathematics, William Andrew, 2016.

[38] C. T. Crowe, Multiphase flow handbook, CRC press, 2005.

[39] Micro-ct images and networks: http://www.imperial.ac.uk/earth-science/research/research-groups/perm/research/pore-scale-modelling/micro-ct-images-and-networks, n.d.

[40] G. Hirasaki, Wettability: fundamentals and surface forces, SPE formation evaluation 6 (1991) 217–226.

[41] C. Hemme, W. Van Berk, Hydrogeochemical modeling to identify potential risks of underground hydrogen storage in depleted gas fields, Applied Sciences 8 (2018) 2282.

[42] R. Groenenberg, J. Koornneef, J. Sijm, G. Janssen, G. Morales-Espana, K. Smekens, Large-scale energy storage in slt caverns and depleted fields, Report, TNO, 2020.

[43] A. S. Voznesenskii, M. N. Krasilov, Y. O. Kutkin, M. N. Tavostin, Y. V. Osipov, Features of inter-relations between acoustic quality factor and strength of rock salt during fatigue cyclic loadings, International Journal of Fatigue 97 (2017) 70–78.

[44] K. R. Kumar, H. Hajibeygi, Multi-scale nonlinear modeling of subsurface energy storage: Cyclic loading with inelastic creep deformation, in: ECMOR XVII, volume 2020, European Association of Geoscientists & Engineers, 2020, pp. 1–13.

[45] A. A. Makhmutov, K. R. Kumar, C. J. Spiers, H. Hajibeygi, Cyclic energy storage in salt caverns: nonlinear finite-element modelling of rock salt creep at reservoir scale, arXiv preprint arXiv:2010.06581 (2020).

[46] A. S. Lord, Overview of geologic storage of natural gas with an emphasis on assessing the feasibility of storing hydrogen, SAND2009-5878, Sandia Natl. Lab. Albuquerque, NM (2009).

[47] S. Foh, M. Novil, E. Rockar, P. Randolph, Underground hydrogen storage. Final report.[Salt caverns, excavated caverns, aquifers and depleted fields], Technical Report, Brookhaven National Lab., Upton, NY (USA), 1979.

[48] H. B. Stone, I. Veldhuis, R. N. Richardson, Underground hydrogen storage in the uk, Geological Society, London, Special Publications 313 (2009) 217–226.

[49] L. Carrette, K. Friedrich, U. Stimming, Fuel cells-fundamentals and applications, Fuel cells 1 (2001).

[50] M. Darzi, C. Park, Optical distortion correction of a liquid-gas interface and contact angle in cylindrical tubes, Physics of Fluids 29 (2017) 052004.

[51] B. H.-P. Cheong, T. W. Ng, Y. Yu, O. W. Liew, Using the meniscus in a capillary for small volume contact angle measurement in biochemical applications, Langmuir 27 (2011) 11925–11929.

[52] H. Lim, M. Lee, J. Lee, Versatile analysis of closed-end capillary invasion of viscous fluids, JMST Advances 1 (2019) 73–79.

A

Validation of experimental apparatus

The setup was successfully calibrated against the existing literature data of Jafari and Jung [8]. They performed microfluidic measurements of advancing and receding contact angles of CO_2/Water at P=10 bar and T=21°C using a chip identical to the chip used in this research. The cleaning method of Jafari and Jung was similar to our cleaning method. In order to match the setup of Jafari and Jung [8], for the first validation test (V1) a setup without filters and valves was used. However, since knowledge was gained about the behaviour and sensitivities of the system (Appendix C), two additional CO_2/water tests (V2 and V3) were performed with the regular setup (presented in 3.2 Figure 3.2). One test was done after saturating the water with CO_2, by filling the pump cylinders with half CO_2 and half$_2$ and leaving it overnight at a pressure of 20 bar. The other test was done with pure water. An overview of all validation tests and the test of Jafari and Jung can be found in Table A.1.

The results of the validation tests are shown in Figure A.1. The orange bars represent the measurements of Jafari and Jung [8] using a similar chip at P=10 bar and T=21°C , the green, yellow and purple bars represent respectively validation experiments V1, V2 and V3, all carried out at P=10 (±1) bar and T=20 (±2) °C.

Figure A.1 shows that the results of experiment V1, using a similar setup, match the results of Jafari and Jung. The deviation is within the experimental error.

Figure A.1 also indicates a clear effect of the filters in the setup on the advancing contact angles. When the system is not properly filtered, presence of contaminants can alter the glass wettability, resulting in an increase of Advancing Contact Angles of up to 45°. Especially when no valves are used, since the system has to be opened and closed for flushing before every experiment, which allows dust to attach on the open wet ends of the tubes. The effect on the receding contact angles is less evident. receding contact angles in unfiltered systems can be up to 5° higher, but this is still within the experimental error.

Lastly, when comparing the results of experiments V2 and V3, it can be seen that saturating the water with CO_2 had no significant influence on the results. This is in line with the finding that even though the water in experiment V1 was not saturated with CO_2, the results are still in agreement with the experiment of Jafari and Jung.

Test Group	**Gas**	**Liquid**	**Rate [µl/min]**	**Tempera-ture [°C]**	**Pressure [bar]**	**Comments**
JJ	CO_2	Saturated Water	0.1	21	10	Setup without filters
V1	CO_2	Pure Water	0.1	20	10	Setup without filters and valves
V2	CO_2	Saturated Water	0.1	20	10	
V3	CO_2	Pure Water	0.1	20	10	

Table A.1: Summary of the validation test Groups. Test Group JJ represents the results of Jafari and Jung [8].

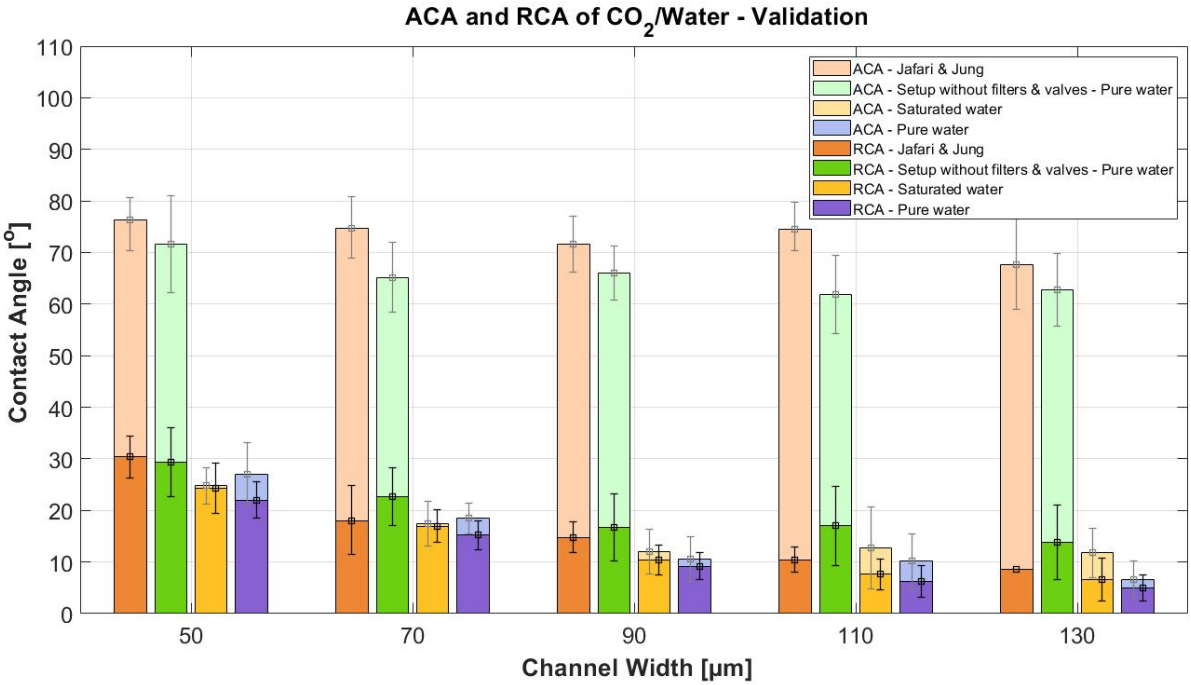

Figure A.1: Advancing and receding contact angles (ACA and RCA) of CO_2 and water. The orange bars represent the results of Jafari and Jung [8] using a similar chip at P=10 bar and T=21°C. The green bars represent results of V1 with a setup similar to Jafari and Jung without filters and valves and pure water, the yellow bars represent the results of V2 with water which was saturated with CO_2 and the purple bars represent the results of V3 with pure water. The error bars represent the standard deviation of the measurements.

B

Validation of image analysis

The image analysis code was validated against the generated specific curvature using MATLAB with the known angles at the contact points. The accuracy of the developed in-house code is $\pm 4°$ which is shown in Figure B.1.

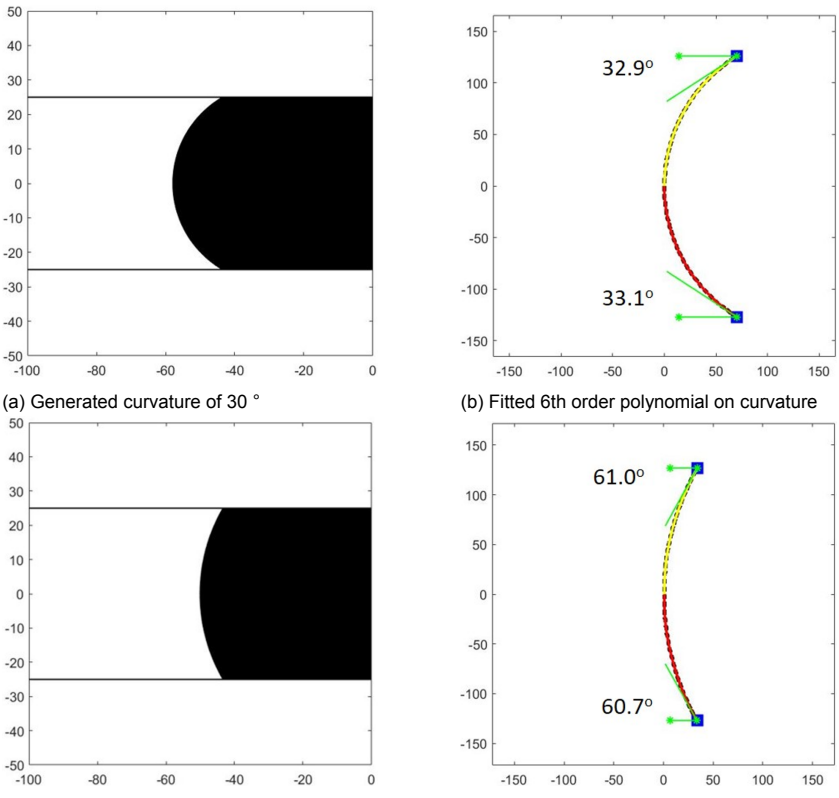

(a) Generated curvature of 30 °

(b) Fitted 6th order polynomial on curvature

(c) Generated curvature of 60 °

(d) Fitted 6th order polynomial on curvature

Figure B.1: Validation of the image analysis with the generated curvature (left) and the fitted polynomial (right).

C

Sensitivity analysis: Contamination

It was found that surface contamination can alter the wettability of the system. This was initially found when unfiltered ethanol was injected and the system became clearly less water-wet. In order to investigate the effect that presence of contaminants can have on the dynamic contact angles, three experiments were performed. For the first test, Chip 1, 2 and 3 were used, which were all injected with the unfiltered ethanol instead of the filtered ethanol during the cleaning procedure. This resulted in severe contamination of the system. Furthermore, the chips were heated up to 400 C in an (unsuccessful) attempt to clean the chip. The second test was done using chip 4. This chip was cleaned with the filtered ethanol, but some tests were done without the inline filters in the gas and water lines (Filters 2 and 3 in Figure 3.2), which caused minor contamination. The third test was done with the unused chip, which was also cleaned with the filtered ethanol. Pictures of these chips can be seen in Figure C.1. All chips were used for tests to investigate the influence of this contamination. Contact angles were only measured if there were no visible contamination particles in the vicinity of the interface.

Figure C.2 shows the results of using different chips. The red bars represent the results of Chip 1-3, the green bars represent the results of chip 4 and the blue bars represent the results of chip 5. All experiments were carried out at P=10 (±1) bar and T=20 (±2) °C.

Figure C.2 indicates a clear effect of contamination on contact angles. It is clear that in chip 1, 2 and 3, significantly higher advancing and receding contact angles were measured compared to chip 4 and 5. The difference between the results of chip 4 and chip 5 is less evident. The receding contact angles are very similar and the deviation are within the range of experimental error. The difference in advancing contact angles is more significant, but in most cases this is within experimental error as well. It is remarkable that the cleanest chip, chip 5, shows a wider range of advancing contact angles than chip 4. This is mainly since during imbibition experiments (measurement of advancing contact angle) in chip 4, almost no water films were observed, while in chip 5 the system was more water-wet because the chip was clean. In this case some interfaces used for advancing contact angle measurement had water films while others did not have a visible water film, like is shown in the pictures in B.1.

Since a clear effect of contamination was found, even though contact angles were not measured within the vicinity of visible pollution, all main experiments were carried out with filters, and only filtered fluids were injected. Furthermore, the system was opened inside the filters minimally in order to prevent dust from coming into the system. Installing valves 2 and 5 (Figure 3.2) enabled this, since the lines did not have to be disconnected for flushing when using valves. The findings of this appendix are in line with the findings of the CO_2 experiments in Appendix A.

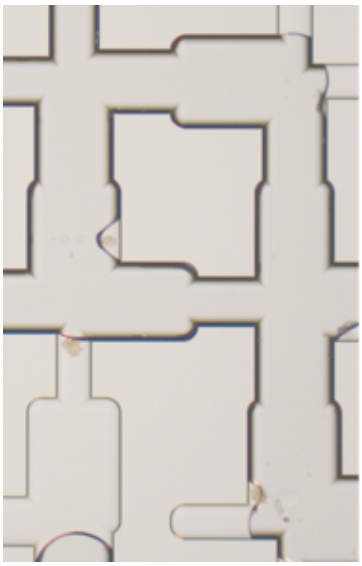

(a) Example of dirt in chip 1, 2 and 3. The chips are severely contaminated and the system is visibly less water-wet and there are no water films present

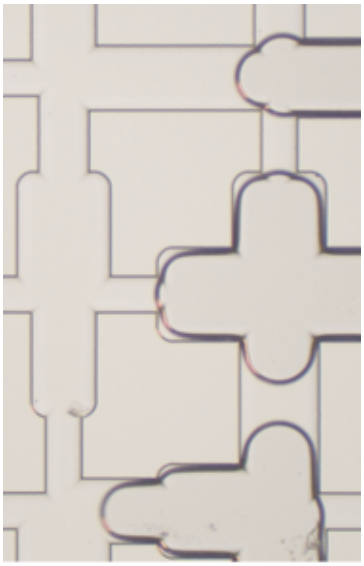

(b) Example of dirt in chip 4. A few dirt particles are visible, but the system is still very water wet and water films are observed

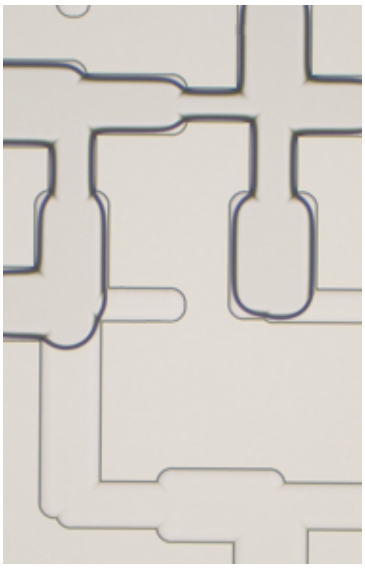

(c) Completely new chip, no dirt visible.

Figure C.1: Examples of contamination and its effect on the wettability

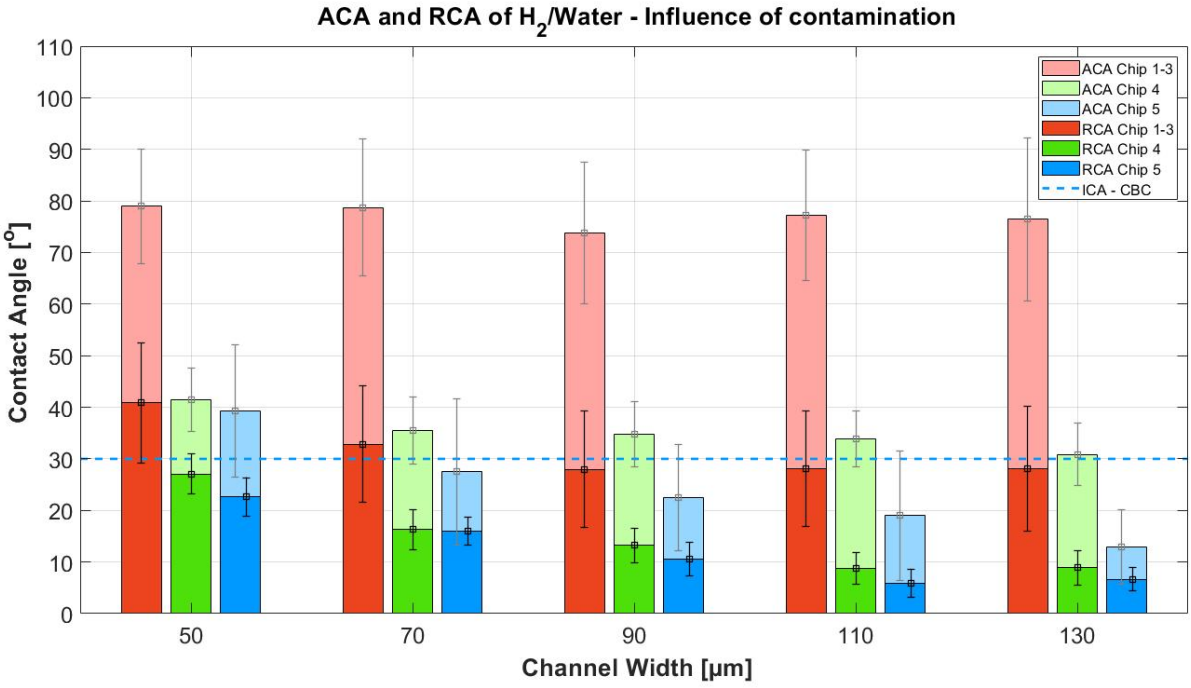

Figure C.2: Advancing and receding contact angles (ACA and RCA) of H_2 and pure water measured at P=10 bar and T=20°C. The red bars represent measurements using chip 1, 2 and 3 which were severely contaminated, The green bars represent measurements using chip 4, which had minor contamination and the blue bars represent measurements using chip 5 which was clean. The dashed blue line represents the results found by Hashemi et al. [3] at P=20 bar and T=20 °C, using the captive bubble cell (CBC). The error bars are the standard deviation of all measurements.

D

Literature study: Disciplines of UHS and main risks

In this section the following disciplines of UHS, as well as its characteristics and its risks are shortly described: Hydrogeology, Geochemistry, Microbiology, Geomechanics and Thermodynamics. An overview of the main risks can be found in Figure D.1.

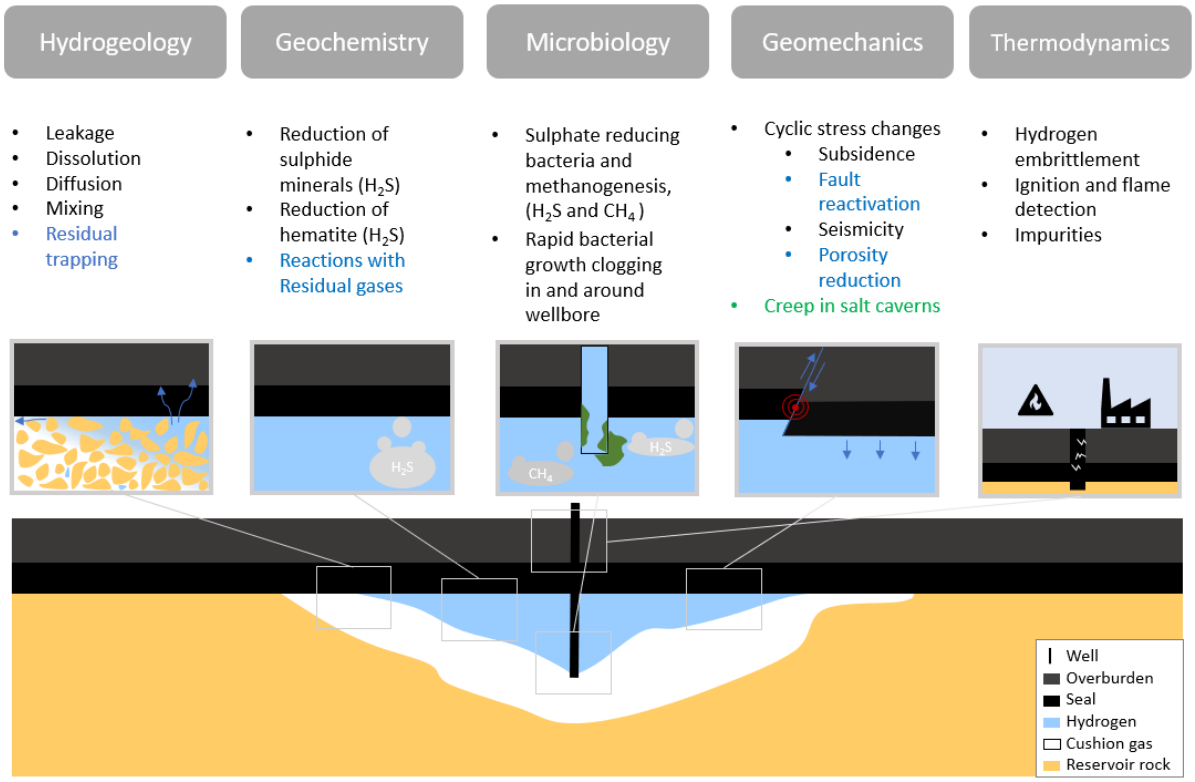

Figure D.1: Overview of the main risks of UHS, with in blue risks which are mainly applicable to depleted oil/gas reservoirs or aquifers and in green risks which are mainly applicable to salt caverns.

D.1. Hydrogeology

Geological formations, such as depleted oil and gas reservoirs, aquifers or salt caverns offer feasible solutions for UHS [5, 10–12]. Depleted oil and gas reservoirs and aquifers consist of porous media. H_2 will be periodically injected and produced and complex multiphase flow patterns between H_2 and the in-

situ fluid (usually brine) will be created [10]. To accurately predict multiphase flow patterns and account for the risks mentioned in this section, data on relative permeability capillary pressure, interfacial tension and contact angle is essential.

H_2 has a relatively low viscosity and therefore a high mobility. Due to its high mobility, H_2 can leak relatively easily through the seal or minor fractures and faults in the seal [41]. Besides that, the high mobility of H_2 in combination with lower-viscosity in-situ fluids present in the reservoir could result in losses because of the lateral spreading of H_2. However, no significant losses are expected due to diffusion [10]. Furthermore, H_2 can dissolve in water, but because of the non-polar nature of H_2, no significant losses of H_2 due to dissolution are expected [10]. Moreover, gases like cushion gas or residual hydrocarbons, could be present in the formation along with H_2. Mixing of the injected H_2 with these gases, causes contamination of stored H_2. The degree of mixing of gasses is strongly depending on the storage type and reservoir properties, the cushion gas used and the cycling, production and injection rates [10]. Lastly, capillary forces cause part of the stored H_2 (residual H_2 saturation) to be irrecoverable, impacting the economic feasibility of the storage project [10].

D.2. Geochemistry

Geochemical reactions can occur in the reservoir between the stored H_2 and the host rock and/or pre-existing reservoir fluids. This could eventually lead to loss in porosity and permeability, and therefore this subject is extensively studied in literature. Hashemi et al. [5] found that most studies report very limited geochemical reactions at moderate reservoir conditions of temperature and pressure, although it was found by both Hashemi et al. [5] and Groenenberg et al. [42] that in pyrite-bearing rocks, Pyrite reduction can lead to H_2S formation, which can affect the economics and facility design, safety and material selection.

Furthermore, the study of Groenenberg et al. [42] reported the following two other geochemical processes which could be a concern for H_2 storage sites: 1) the reduction of hematite to magnetite, by sequestering H_2 can produce H_2O, which can lead to the need of additional surface facilities and 2) the presence of additional (residual) gases such as CO_2 can lead to changes in the fluid composition and pH, possibly resulting in precipitation and dissolution of secondary minerals, and degrading reservoir performance.

D.3. Microbiology

Microbial activities are a risk for subsurface storage of H_2. The two most relevant processes are bacterial sulphate reduction (D.1) and methanogenesis (D.2) [41].

$$\text{bacterial sulfate reduction}: \mathrm{SO_4^{2-}_{(aq)}} + 5\mathrm{H_{2(aq)}} \rightarrow \mathrm{H_2\ S_{(aq)}} + 4\mathrm{H_2O} \tag{D.1}$$

$$\text{methanogenesis:}\ \mathrm{CO_{2(aq)}} + 4\mathrm{H_{2(aq)}} \rightarrow \mathrm{CH_{4(aq)}} + 2\mathrm{H_2O} \tag{D.2}$$

In both processes H_2 is catalyzed by bacteria, and converted to H_2S or CH_4 and water. Mainly H_2S is a risk factor because it is toxic when inhaled, it can cause damage to the storage facilities and can be harmful for the environment. The activity of the bacteria is highly depending on the availability of electron acceptors like sulphate and carbon dioxide and the temperature [41]. Rapid bacterial growth may cause clogging in and near the wellbore [42].

D.4. Geomechanics

Cyclic injection and production of H_2 leads to cyclic pressure changes on both intact rocks and faults. Heinemann et al. [10] found in a literature study that cyclic stress and temperature fluctuations can lead to reservoir compaction, causing porosity reduction, subsidence, fault reactivation and potential seismicity.

Although cyclic loading is extensively studied, very few studies have been conducted specifically for underground gas storage, of which most of them are specified on storage in salt caverns. For example, Voznesenskii et al. [43] studied the strength of rock salts under cyclic loads for the application of using rock salt as a storage medium for hydrocarbons and other gasses. It was found that the strength of the rock salt undergoes a non-monotonous change under the number of cycles loads. Kumar and Hajibeygi [44] presented a computational framework for cyclic loading with inelastic creep deformation

to model subsurface energy storage. It was concluded that nonlinear deformation is an important aspect of seasonal energy storage. Makhmutov et al. [45] modelled complex creep behaviour in salt caverns used for cyclic storage of H_2. After several years creep in salt caverns becomes evident and could eventually lead to failure of the structural integrity of the cavern. Studies about cyclic loading in porous media for gas storage are not yet found in literature.

More research on cyclic loading of subsurface energy storage is needed for a better understanding of the complex processes involved in subsurface energy storage. Understanding these complex processes is essential to guaranty the safety, reliability and feasibility of UHS on the long term [44].

D.5. Thermodynamics

H_2 has a critical temperature of -239.97 °C, a critical pressure of 1.297 MPa and is stored in gaseous phase at typical reservoir conditions. The viscosity of H_2 is low compared to CH_4 and CO_2 in typical subsurface conditions and is relatively stable under changing pressure and temperature [10].

H_2 has a much wider flammability range compared to methane. Furthermore, a H_2 flame gives little sensation of heat, because of a lack of IR radiation, but exposure to an H_2 flame can cause severe burns because of UV radiation [42]. H_2 embrittlement, the effect that H_2 can have on the mechanical and physical properties of metals, can be a large concern in the field of underground H_2 storage. H_2 embrittlement can affect the integrity of the surface and subsurface facilities, and the type of steel must therefore be carefully selected [46, 47].

It is likely that H_2 does not stay fully pure during storage, because it is a highly reactive gas. As mentioned in the previous sections, additional gasses like H_2S can be produced when H_2 is stored in porous media, because of biochemical and geochemical reactions. The thermo-physical properties of impure H_2 differs significantly from pure H_2, and therefore mixing with other gases could lead to operational issues [10]. For example, when the H_2 is used in a fuel cell, processing steps are necessary in order to purify the H_2 [48]. This purification process is essential, because impurities in H_2 decrease the efficiency of the fuel cells [49].

E

Capillary Tube Experiment

Microfluidic chips resemble actual subsurface systems much closer than tilted plate techniques or captive bubble cells, because of the dynamic and micro-channel-based nature of the flow conditions. However, a wide range of contact angles per channel width is observed. One of the reasons for this wide range, is the difference in local velocity, pressure and flow regimes at the specific place where the dynamic contact angle was measured. Using capillary tubes for measuring dynamic contact angles in a H_2/water/glass system, gives the opportunity to have direct influence on the local velocity, pressure and flow regime of the measurement. It is therefore expected to result in a smaller range of measurements, even though they are less representative for actual pore networks.

As part of this master thesis, a capillary tube setup was designed to measure dynamic contact angles in a H_2/water/glass system. However, due to difficulties in imaging, it was chosen to continue using microfluidic chips. This section describes the knowledge gained on measuring dynamic contact angles in capillary tubes and processing the images.

E.1. Experimental Apparatus

Figure E.1 provides a schematic overview of the microfluidic apparatus. The camera is a Canon EOS 70D in combination with a Macro Photo Lens MP-E 65 mm. The pump is a Quizix QX6000 cylinder pump. The valves installed (Swagelok) are 1/8" and transparent tubes are used. A back light is used to obtain well-lighted images. The experimental apparatus was planned to be calibrated against the data of Li et al. [22], who measured dynamic contact angles of a water/air system in glass capillary tubes (ID=100-250 µm).

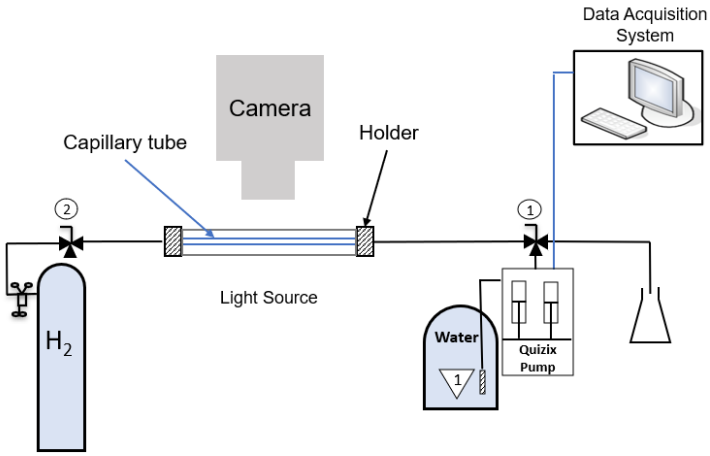

Figure E.1: Schematic drawing of the experimental apparatus used to measure dynamic contact angles in capillary tubes.

E.2. Materials

Borosilicate circular capillary tubes with inner diameter (ID) ranging from 50 to 1000 µm and outer diameter (OD) of 6.2 or 8.0 mm is used. A pure quartz tube is used determine the influence of glass types on dynamic contact angles. It is chosen to use round capillary tubes to avoid influence of corner effects. The maximum pressure of the tubes is 100 bar, because of their small ID relative to OD. The tubes of 250 µm ID and smaller are most important for benchmarking because of the dominancy of capillary forces.

E.3. Refraction of light creating distorted image

The H_2/water interface inside capillary tubes appear distorted as light gets refracted passing due to different media. Such distortion may cause significant errors on measuring contact angles in capillary tubes [50]. The refraction effect is visualized in Figure E.2. Point 1, 2 and 3 appear as point 1',2' and 3', so the image appears wider than it actually is. Therefore contact angles are significantly influenced by this effect.

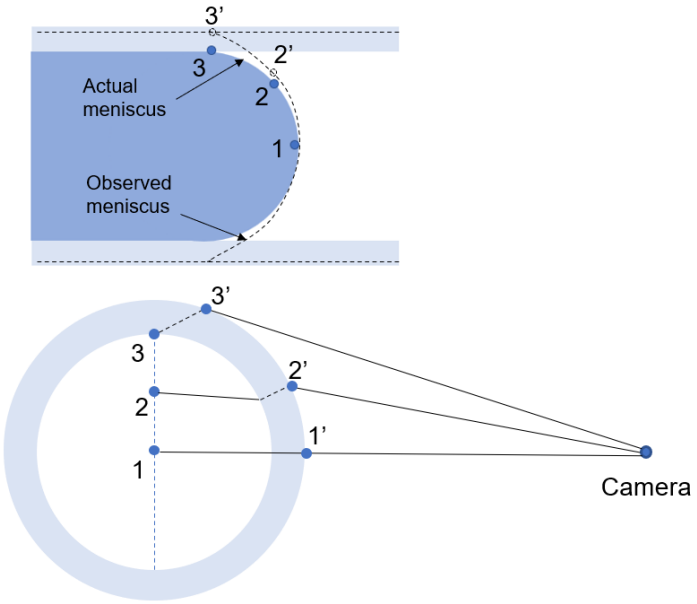

Figure E.2: Schematic drawing of refraction of light in circular tubes. Top: view parallel to tube; Bottom: view perpendicular to tube.

To obtain representative results, it is necessary to correct for these effects. Three different methods were tested against existing of literature of Al-Zaidi and Fan [24] on air/water static contact angles in capillary tubes using tube ID's in the range of 50 to 1000 µm.

- *Method based on Darzi and Park [50]*

  Darzi and Park [50] created a method for point-by-point correction for distortion of points based on the refraction indices of air, glass and water, which is presented in Figure E.3a. The method requires: 1) a measurement of distance from camera until the middle point of the tube, 2) a scale within the image which is not distorted (perpendicular to the flow direction), 3) ID and OD of the tube, 4) refractive indices of the glass, air and water, 5) vertical distance of apparent point to mid-tube. This method is theoretically very accurate but in practice there is too much error involved in the measurements to successfully complete this process.

- *Method based on Cheong et al. [51] and Lim et al. [52]*

  Cheong et al. [51] and Lim et al. [52] both developed a method based on the assumption that the interface can be fit by a circle, like shown in Figure E.3b. In this method, only the capillary height needs to be measured and from there the contact angle can be calculated. Using this method, it was possible to match the literature [24] by ±7 °.

- *Squeezing image based on known ID*

  If we assume that the distortion of the image is linear from the center of the tube towards the wall of the tube it is possible to squeeze the image until the ID of the tube in picture matches the actual ID of the tube. In order to do this, a non-distorted scale (for example OD) needs to be used to squeeze the image to the right size (Figure E.3c). Using this method, it was possible to match the literature [24] by ±7 °, just like the method of Cheong et al. [51] and Lim et al. [52]

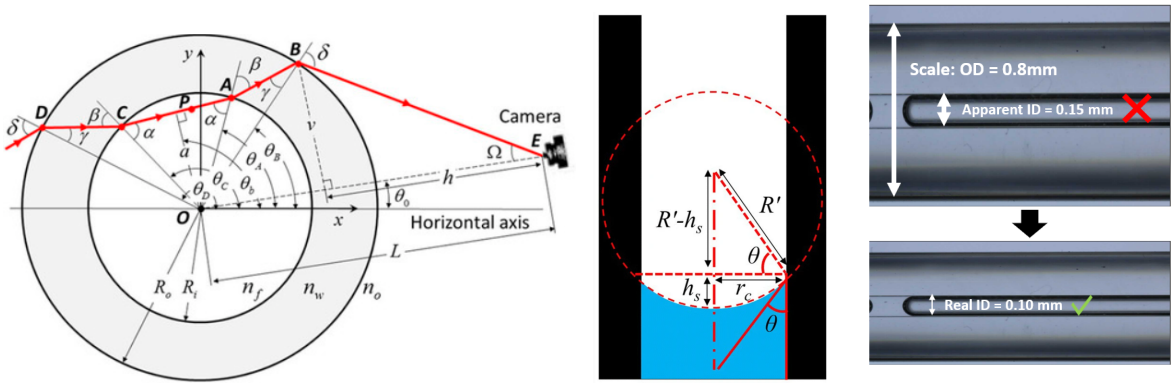

(a) Method proposed by Darzi and Park [50].

(b) Method proposed by Cheong et al. [51] and Lim et al. [52].

(c) Method based on known ID.

Figure E.3: Methods used for correction of image distortion.

E.4. Technical Challenge: Sharpness of images

Obtaining sharp images of the H_2/water interface for tubes with ID's smaller than 200 µ was challenging. In order to get sharper images the lens of the camera used was replaced by a microscope: the Leica MZ8. The Canon EOS 70D was attached to this microscope by using a C-mount. Using this microscope, still no sharp images could be obtained.

One of the reasons for these blurred images was the refraction of light on the curved surface. Because glycerol has a refraction coefficient similar to glass, the sharpness of the image was significantly improved by putting the tube in a box with glycerol. The light then enters the glycerol on a flat surface and is therefore not refracted. Due to the similar refraction coefficient of glass and glycerol, light is also not significantly refracted at the glass/glycerol interface. A test was also done with water, because the refraction coefficient of water is closer to glass than air, a positive effect on the sharpness of the image was also observed (Figure E.4).

However, the images in Figure E.4c were still not sharp enough for the MATLAB script as explained in section 3.4. ImageJ was used to visually fit a tangent line, but this method is very sensitive to the accuracy of the analyzer and resulted in an inaccuracy of ±10 °.

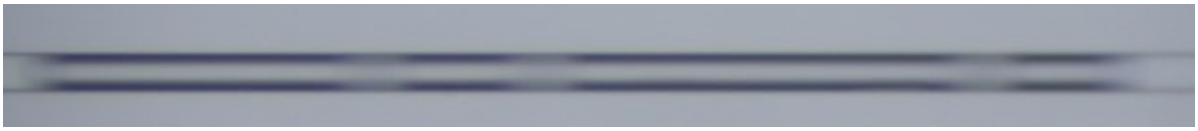

(a) Imaging through air

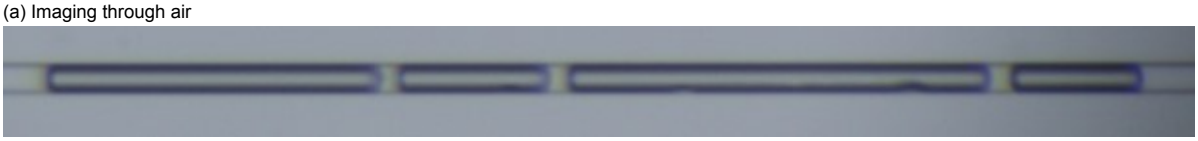

(b) Imaging through water

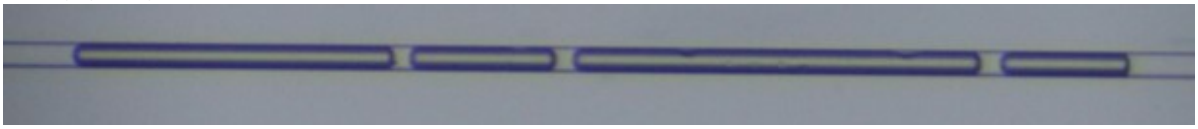

(c) Imaging through glycerol

Figure E.4: Images of capillary tube setup through air, water and glycerol.

E.5. Future recommendations

The following options can be considered to continue with this experimental setup:

- *DFC7000T from the microfluidic setup*

  This microscope has lenses with bigger magnification and therefore it would be easier to obtain sharp images. However, this microscope is mainly suitable for 2D imaging, like microchips and therefore the objects have to be placed very close to the lens.

- *Tube in glycerol and usage ImageJ for image analysis*

  As explained in the section above, placing the tube in glycerol and using ImageJ for image analysis is possible but leads to high inaccuracy of ±10°.

- *Experiments at ambient conditions*

  If experiments are only performed at ambient conditions, new tubes with a thinner glass wall (smaller OD) could be purchased. Tubes with a thinner glass wall allow for less light refraction. However, these tubes are also not able to withstand high pressures due to their thin walls.

- *Microchips with single channels*

  The microchip setup in Figure 3.2 gives reliable results with channel widths between 50 to 130 µm. Therefore, it is an option to use microchips with straight channels. However, microchips are manufactured with square instead of circular channels and for this reason the corner effects need to be accepted.

F

Detailed experimental procedure

The general experimental procedure is described in Section 3.3 and the experimental apparatus is shown in Figure 3.2. This section lists all the steps of the experimental procedure in detail. First the steps of the cleaning procedure are listed, followed by the procedure for drainage tests and lastly, the steps for the procedure of the imbibition tests are described.

Cleaning procedure:

- Rinse Quizix pump – Completely extending both cylinders of the Quizix (10 ml/min) pump using the outlet directly at the quizix pump;
- Set valve 2 to outlet and rinse chip with water for 5 min (0.6 ml/min) using the Quizix pump;
- Connect outlet of valve 2 to the ethanol flask;
- Set valve 5 towards the outlet;
- Rinse chip with 5 mL of filtered ethanol;
- Remove the ethanol flask from the outlet of valve 2;
- Connect the N_2 network line to the outlet of valve 2 and dry the chip by flushing extensively with filtered N_2;
- Set valve 2 toward the H_2 cylinder and flush the dried chip with H_2 to remove N_2.

Directions of valves before starting an experiment:

- Valve 1 is closed;
- Valve 2 is set towards the H_2 cylinder;
- Valve 5 is set towards the pumps;
- Valve 6 is open.

Drainage procedure (measurement of receding contact angle):

- Switch valve 2 towards the outlet and flush the chip using the Quizix pump with water until (almost) no H_2 is visible in the chip;
- Switch valve 2 towards the H_2 cylinder;
- Set the pressure regulator of the cylinder at required pressure and open valve 1 to pressurize the system;
- Use the Quizix pump to retract water at the flow rate of 0.1 mL/min until a moving interface is observed in the line between connection point 2 and 3;

- Stop the Quizix pump and close valve 6. Check if the interface is stable. A moving interface indicates a leak in the system;
- Retract water with the syringe pump until H_2 reaches the chip. When the interface reaches point 3, use a flow rate of 0.001 mL/min;
- Use the 1.25 x lens on the microscope to observe when H_2 enters the chip. When H_2 movement is observed in the chip, directly set the required flow rate of 0.1µL/min, switch to the 10 x lens of the microscope and start a video.

Imbibition procedure:

- Flush the chip with water using the Quizix pump until (almost) no H_2 is visible in the chip by setting valve 2 to outlet and valve 5 towards the chip;
- Switch valve 2 towards the chip and set valve 5 towards outlet;
- Flush H_2 through the chip, until the water inlet of the chip is dry enough;
- Switch valve 5 towards the pumps, set the pressure regulator of cylinder at the required pressure and open valve 1;
- Use the Quizix pump to inject water at the flow rate of 0.1 mL/min until a moving interface is observed in the line between connection point 4 and 5;
- Stop the Quizix pump and close valve 6. Check if the interface is stable. A moving interface indicates a leak in the system;
- Inject water using the syringe pump until the H_2/water interface reaches the chip. When the interface reaches point 4, use a flow rate of 0.001 mL/min;
- Use the 1.25 x lens on the microscope to observe when water enters the chip. When water movement is observed in the chip, directly set the required flow rate of 0.1µL/min, switch to the 10 x lens of the microscope and start a video.